

WOMBAT: A fully Bayesian global flux-inversion framework

Andrew Zammit-Mangion*

School of Mathematics and Applied Statistics,
University of Wollongong, Australia

Michael Bertolacci*

School of Mathematics and Applied Statistics,
University of Wollongong, Australia

Jenny Fisher

School of Earth and Life Sciences, University of Wollongong, Australia

Ann Stavert

Climate Science Centre, CSIRO Oceans and Atmosphere, Australia

Matthew L. Rigby

School of Chemistry, University of Bristol, UK

Yi Cao

School of Mathematics and Applied Statistics,
University of Wollongong, Australia

Noel Cressie

School of Mathematics and Applied Statistics,
University of Wollongong, Australia

Abstract

WOMBAT (the Wollongong Methodology for Bayesian Assimilation of Trace-gases) is a fully Bayesian hierarchical statistical framework for flux inversion of trace gases from flask, *in situ*, and remotely sensed data. WOMBAT extends the conventional Bayesian-synthesis framework through the consideration of a correlated error term, the capacity for online bias correction, and the provision of uncertainty quantification on all unknowns that appear in the Bayesian statistical model. We show, in an observing system simulation experiment (OSSE), that these extensions are crucial when the data are indeed biased and have errors that are correlated. Using the GEOS-Chem atmospheric transport model, we show that WOMBAT is able to obtain posterior means and uncertainties on non-fossil-fuel CO₂ fluxes from Orbiting Carbon Observatory-2 (OCO-2) data that are comparable to those from the Model Intercomparison Project (MIP) reported in Crowell et al. (2019, *Atmos. Chem. Phys.*, vol. 19). We also find that our predictions of out-of-sample retrievals from the Total Column Carbon Observing Network are, for the most part, more accurate than those made by the MIP participants. Subsequent versions of the OCO-2 datasets will be ingested into WOMBAT as they become available.

Keywords: Bayesian Hierarchical Model; Carbon Cycle; Markov Chain Monte Carlo; Physical-Statistical Model; Spatio-Temporal Statistics.

*Contributed equally

1 Introduction

Carbon dioxide (CO_2) is a leading driver of global warming (Peters et al., 2013). If left unchecked, the rise in global temperatures will have a substantial negative impact on society and the environment (Edenhofer et al., 2014). As part of the worldwide effort to limit these impacts, the 2016 Paris Agreement under the United Nations Framework Convention on Climate Change, COP 21, called for a global stocktake of the sources and sinks of CO_2 and other greenhouse gases, with the first evaluation planned for 2023 (UNFCCC, 2015). The rate at which CO_2 is emitted (from sources) or absorbed (at sinks) per unit space and time is known as the CO_2 flux, which itself varies substantially spatio-temporally. Despite the fact that it is human emissions that are driving the rise in atmospheric CO_2 concentrations, these emissions are relatively easy to quantify, and the most uncertain aspects of quantifying CO_2 fluxes at Earth’s surface centre around natural processes. For example, while we know that the land and ocean absorb more than half of the CO_2 emitted by human activities (Dlugokencky and Tans, 2020), the geographical and temporal patterns of these sinks remain unclear (Crowell et al., 2019).

Monitoring the progression of CO_2 in our atmosphere is thus of utmost importance, and billions of dollars have been spent over the last few decades on research, development, and deployment of instruments for measuring CO_2 mole fraction (defined here as the proportion of CO_2 molecules in a given parcel of dry air) on a global scale (Burrows et al., 1995; Kuze et al., 2009; Wunch et al., 2011a; Masarie et al., 2014; Eldering et al., 2017, 2019). However, CO_2 mole fraction is only indirectly related to the key quantity of interest, namely the geographic distribution of the CO_2 fluxes, which cannot be observed directly on regional scales. Identifying these sources and sinks is an ill-posed inverse problem, often called a trace-gas flux-inversion problem, whose solution requires the use of both an atmospheric transport model and a spatio-temporal model for the fluxes (e.g., Enting, 2002). In this paper, we present a global flux-inversion system for the solution of this problem, which we call the Wollongong Methodology for Bayesian Assimilation of Trace-gases (WOMBAT).

A global trace-gas flux-inversion system is designed to infer fluxes from observational data, which are generally available either as point-referenced (flask or *in situ*) measurements or column-averaged remote-sensing retrievals. The underlying model in an inversion system is usually a state-space model, where the fluxes, or a reduced representation thereof, are the latent states that need to be inferred from data via the use of an atmospheric chemical transport model (CTM). Computationally, flux estimation is either done within a standard optimisation framework (e.g., Chevallier et al., 2005; Baker et al., 2006), via full Bayesian synthesis (Enting 2002, Chapter 3; Mukherjee et al. 2011; Schuh et al. 2019), or via ensemble Kalman filtering (e.g., Peters et al., 2005; Feng et al., 2009). Inversion systems rely, to various extents, on realistic bottom-up estimates of fluxes for the elicitation of an informative prior distribution; an accurate CTM that provides the link between the fluxes and the observed mole fraction; high-quality unbiased measurements; and reliable uncertainty measures on each model component.

The complexity of all modelled processes, from fluxes right up to satellite retrieval errors, inevitably leads to model misspecification. Further, because flux inversion is an ill-posed problem, even if the misspecification is slight, the consequences for model-based flux estimates could be significant (e.g., Enting and Newsam, 1990), and they can lead to a large spread in posterior flux estimates from different flux-inversion systems. Hence, uncertainty from an ensemble of inversions is usually quantified through the spread of the posterior means from different inversion systems, rather than through the application of a meta-analysis that takes into account statistical uncertainties of individual estimates (e.g., Houweling et al., 2015; Crowell et al., 2019; Rayner, 2020). The large disagreements between inversion results suggests that at least some inversion systems are missing (or have misspecified) certain components of variability in their underlying models.

The causes of model misspecification are numerous; for a comprehensive discussion, see Engelen et al. (2002). The main ones are (i) flux-process dimension-reduction error (e.g., Kaminski et al., 2001), which is a consequence of using a spatio-temporal model for the flux field that is low-dimensional and inflexible; (ii) an inaccurate prior flux mean, variance, and covariance (e.g., Philip et al., 2019); (iii) transport-model errors (e.g., Houweling et al., 2010; Basu et al., 2018; Schuh et al., 2019) arising from the underlying assumed physics, meteorology, and discretisation schemes used (e.g., Lauvaux et al., 2019; McNorton et al., 2020); (iv) retrieval biases (e.g., O’Dell et al., 2018) and incorrect associated measurement-error statistics (e.g., Worden et al., 2017); and (v) measurement-error spatio-temporal correlations that are not fully accounted for (e.g., Chevallier, 2007; Ciais et al., 2010). Two other causes of model misspecification worth noting are an

incorrectly specified initial global mole-fraction field, and flux components assumed known in the inversion (i.e., assumed degenerate at their prior mean), such as anthropogenic emissions (e.g., Feng et al., 2019). The latter can be seen as a special case of (i) above, while the effect of the former can generally be minimised by using a realistic initial condition (e.g., Basu et al., 2013) and incorporating a burn-in (or spin-up) period, in which early flux estimates are discarded.

In Section 2 we present the underlying framework of WOMBAT. The statistical framework addresses the implications of model misspecification in several ways: first, by using prior distributions to encode uncertainty over prior beliefs on the fluxes (e.g., Ganesan et al., 2014; Zammit-Mangion et al., 2016); second, by adding a spatio-temporally correlated component of variability to the mole-fraction data model to address some of this typically unmodelled, correlated model–data discrepancy (Brynjarsdóttir and O’Hagan, 2014); third, by explicitly modelling biases in the mole-fraction data model (generalising the approach of Basu et al., 2013); and fourth, by propagating uncertainty on all unknowns within a fully Bayesian statistical framework wherein inference is made using Markov chain Monte Carlo (MCMC). We note that while the benefits of MCMC are becoming increasingly apparent in *regional* trace-gas inversions (e.g., Mukherjee et al., 2011; Ganesan et al., 2014; Miller et al., 2014; Zammit-Mangion et al., 2016), its use is still the exception rather than the rule in *global* trace-gas inversions.

The fully Bayesian nature of the model, coupled with the introduction of a correlated process in modelling the mole-fraction field, leads to computational challenges. Section 3 details how we deal with these by defining a specific type of stochastic process on the irregularly located spatio-temporal errors, one that leads to a sparse precision matrix (Vecchia, 1988; Datta et al., 2016). Details on how this facilitates the MCMC scheme we implement are deferred to Appendix A. Section 4 discusses the experimental setup used for running, validating, and implementing WOMBAT on the satellite data analysed in this article. In Section 5, we first conduct an observing system simulation experiment (OSSE) in which the true fluxes are assumed known. Results from the OSSE demonstrate WOMBAT’s validity and also illustrate the importance of modelling biases and correlated error terms when these are indeed present in the data. We then use WOMBAT to perform flux inversion using the Orbiting Carbon Observatory-2 (OCO-2) Version 7 retrospective (V7r) dataset as used in the model intercomparison project (MIP) of Crowell et al. (2019). Our model fitting reveals that about 80% of the total measurement-error variance associated with the data used for the MIP can be explained with a correlated model–data discrepancy term. WOMBAT accounts for this, which results in posterior distributions over the fluxes that, for the most part, corroborate the results from the ensemble inversions, both on a regional and on a global scale. In Section 5, we also show the utility of WOMBAT in carrying out online bias correction. Section 6 summarises the features of WOMBAT and discusses avenues for future work. Code reproducing the analyses is available online at <https://github.com/mbertolacci/wombat-paper/>.

2 Bayesian hierarchical model for global flux inversion of trace gases

In this section we outline the spatio-temporal Bayesian hierarchical statistical model (see, for example, Wikle et al., 2019, Section 1.3) that WOMBAT uses for global flux inversion. The model consists of four sub-models: (1) a flux process model, (2) a mole-fraction process model, (3) a mole-fraction data model, and (4) a parameter model.

2.1 The flux process model

Let $Y_1^0(\mathbf{s}, t)$ denote the prior mean of the trace-gas surface flux at spatial location $\mathbf{s} \in \mathbb{S}^2$ and time $t \in \mathcal{T}$, where \mathbb{S}^2 is the surface of Earth, and $\mathcal{T} \equiv [t_0, t_f]$ is some time interval of interest. The field $Y_1^0(\cdot, \cdot)$ could be set to zero everywhere (e.g., Michalak et al., 2004) or could be constructed using bottom-up estimates of biospheric and/or anthropogenic fluxes (e.g., Basu et al., 2013).

In the vein of conventional Bayesian-synthesis frameworks (e.g., Enting, 2002), we model the *true* flux, $Y_1(\cdot, \cdot)$, as $Y_1^0(\cdot, \cdot)$ plus a spatio-temporal field that consists of two components. The first component, the *structured* component, is the sum of r spatio-temporal basis functions that are not necessarily disjoint in space and time. These basis functions could be space-time step functions, as typically found in variational

inversion systems (e.g., Chevallier et al., 2005), discretised flux ‘patterns’ (e.g., Fan et al., 1998), or they could be a general-purpose basis such as a Fourier basis (e.g., Crowell et al., 2019, Appendix A4). The second component of $Y_1(\cdot, \cdot)$ is an error arising from the use of a low-dimensional model for the first component and is commonly termed aggregation error; here we call it dimension-reduction error. This error accounts for the fact that the structured basis functions typically span a small (function) space, and therefore they cannot reproduce fluxes perfectly. In practice, these errors correspond to sub-grid-cell flux variation or, more generally, to variations at smaller scales than the basis functions can resolve.

Denote the set of pre-specified flux basis functions as $\{\phi_j(\cdot, \cdot) : j = 1, \dots, r\}$, and the dimension-reduction error component as $v_1(\cdot, \cdot)$. Our flux process model is a spatio-temporal stochastic process given by,

$$Y_1(\mathbf{s}, t) = Y_1^0(\mathbf{s}, t) + \sum_{j=1}^r \phi_j(\mathbf{s}, t) \alpha_j + v_1(\mathbf{s}, t), \quad \mathbf{s} \in \mathbb{S}^2, t \in \mathcal{T}, \quad (1)$$

where the scaling factors $\{\alpha_j : j = 1, \dots, r\}$ are unknown, are assigned a multivariate probability distribution, and need to be inferred in the inversion framework. The error process $v_1(\cdot, \cdot)$ is also unknown but, as we will discuss later, it is not possible to estimate it in isolation of other components of error that appear in other layers of the hierarchical statistical model.

Since we assume that $E(Y_1(\cdot, \cdot)) = Y_1^0(\cdot, \cdot)$, we let $E(\alpha_j) = 0$ for $j = 1, \dots, r$, and $E(v_1(\cdot, \cdot)) = 0$. For a given set of basis functions, the prior belief on the covariance structure of $Y_1(\cdot, \cdot)$ is fully determined by that on $\boldsymbol{\alpha} \equiv (\alpha_1, \dots, \alpha_r)'$ and that on $v_1(\cdot, \cdot)$. Reasonable prior judgements for the moments of both of these will in turn largely depend on the choice of basis functions. For example, when the flux is modelled on a space-time grid and space-time step functions are used as basis functions, a prior distribution on $\boldsymbol{\alpha}$ that correlates the flux *a priori* in space and time is natural (Michalak et al., 2004; Chevallier et al., 2007; Basu et al., 2018). On the other hand, when using large spatial flux ‘patterns’ that have temporally-limited scope, it is generally reasonable to assume that the α_j ’s corresponding to basis functions in different spatial regions are uncorrelated, but that those associated with the same spatial region are temporally correlated.

Irrespective of the choice of basis functions, in WOMBAT one expresses prior judgement on $\boldsymbol{\alpha}$ through the model $\boldsymbol{\alpha} \sim \text{Gau}(\mathbf{0}, \boldsymbol{\Sigma}_\alpha)$, where $\text{Gau}(\boldsymbol{\mu}, \boldsymbol{\Sigma})$ is the Gaussian probability density function of a random vector with mean $\boldsymbol{\mu}$ and covariance matrix $\boldsymbol{\Sigma}$. The covariance matrix $\boldsymbol{\Sigma}_\alpha$ is parameterised through a parameter vector $\boldsymbol{\theta}_\alpha$, which typically contains variances and spatio-temporal length scales in the covariances. Expert elicitation can be used to construct prior distributions on these parameters too; we describe possible prior distributions when discussing the parameter model in Section 2.4.

It is harder to formulate prior beliefs on the process $v_1(\cdot, \cdot)$, but it is reasonable to claim that this process has strictly positive variance and is spatio-temporally correlated. For this reason, it is natural to model $v_1(\cdot, \cdot)$ as a spatio-temporal Gaussian process (e.g., Rasmussen and Williams, 2006) with zero expectation. However, as mentioned above, we temporarily set aside describing its covariance function. Instead we see what impact this term can be expected to have on the mole-fraction field and its consequent process model, and then we model the spatio-temporal discrepancies of all possible contributors to model–data discrepancy together (Section 2.3).

2.2 The mole-fraction process model

Denote the true mole-fraction process at space-height-time location (\mathbf{s}, h, t) as $Y_2(\mathbf{s}, h, t)$. We only model the mole fraction within our time interval of interest, \mathcal{T} , and therefore we express the true mole fraction field within \mathcal{T} as a function of the initial mole-fraction process at t_0 and the exogenous flux-process inputs in \mathcal{T} . Specifically, define $\mathcal{T}_t \equiv [t_0, t]$, for $t_0 \leq t \leq t_f$, as the set of all time points in \mathcal{T} up to and including t . The field $Y_2(\cdot, \cdot, \cdot)$ is related to the flux process through the relationship,

$$Y_2(\mathbf{s}, h, t) = \mathcal{H}(Y_2(\cdot, \cdot, t_0), Y_1(\cdot, \mathcal{T}_t); \mathbf{s}, h, t), \quad \mathbf{s} \in \mathbb{S}^2, h \in \mathbb{R}^+, t \in \mathcal{T}, \quad (2)$$

where $Y_2(\cdot, \cdot, t_0)$ is the mole-fraction field at time t_0 , $Y_1(\cdot, \mathcal{T}_t)$ is the flux field evolving over the whole time period \mathcal{T}_t , and \mathcal{H} is an operator that solves the underlying chemical transport equations (that are approximately linear for long-lived species such as CO_2 ; see, e.g., Enting, 2002, Chapter 2). In practice, \mathcal{H} is not known perfectly, but we usually have at hand a reasonable approximation to it, $\hat{\mathcal{H}}$, which is often

referred to as the chemical transport model (CTM) or simply as the transport model. Similarly, we will usually have a reasonable approximation to $Y_2(\cdot, \cdot, t_0)$, which we call $\hat{Y}_2(\cdot, \cdot, t_0)$. The use of $\hat{Y}_2(\cdot, \cdot, t_0)$ instead of $Y_2(\cdot, \cdot, t_0)$, and of $\hat{\mathcal{H}}$ instead of \mathcal{H} , leads to a residual term $v_2(\cdot, \cdot, \cdot)$ that will inevitably be spatio-temporally correlated (Enting, 2002, Chapter 9). In particular,

$$Y_2(\mathbf{s}, h, t) = \hat{\mathcal{H}}(\hat{Y}_2(\cdot, \cdot, t_0), Y_1(\cdot, \mathcal{T}_t); \mathbf{s}, h, t) + v_2(\mathbf{s}, h, t), \quad \mathbf{s} \in \mathbb{S}^2, h \in \mathbb{R}^+, t \in \mathcal{T}, \quad (3)$$

where $v_2(\cdot, \cdot, \cdot)$ is the residual mole-fraction process arising from the use of an approximate initial mole-fraction field, imperfect meteorology inside the transport model, imperfect transport-model parameters and physics, and potentially sub-grid-scale variation in the mole-fraction when $\hat{\mathcal{H}}$ is a numerical model evaluated at a coarse resolution. It is difficult to place prior beliefs on the structure of $v_2(\cdot, \cdot, \cdot)$, which we model as statistical error, but it is known that using the approximation $\hat{\mathcal{H}}$ introduces errors that could span hundreds of kilometres and several days (Lauvaux et al., 2019; McNorton et al., 2020). Transport-model implementations tend to differ considerably in their vertical and inter-hemispheric mixing behaviour, and flux-inversion estimates are known to be particularly sensitive to transport-model choice (Gurney et al., 2002; Schuh et al., 2019). Note that $v_2(\cdot, \cdot, \cdot)$ is also likely to depend on $Y_1(\cdot, \cdot)$, and that we ignore this dependence for model simplicity in what follows.

The assumed linear behaviour of the underlying dynamics for CO_2 is important. First, it allows us to model the effect of the approximate initial mole-fraction field, $\hat{Y}_2(\cdot, \cdot, t_0)$, separately from that of the fluxes (e.g., Enting, 2002, Chapter 10), so that (3) is of the form

$$Y_2(\mathbf{s}, h, t) = \hat{\mathcal{H}}(\hat{Y}_2(\cdot, \cdot, t_0), 0; \mathbf{s}, h, t) + \hat{\mathcal{H}}(0, Y_1(\cdot, \mathcal{T}_t); \mathbf{s}, h, t) + v_2(\mathbf{s}, h, t), \quad \mathbf{s} \in \mathbb{S}^2, h \in \mathbb{R}^+, t \in \mathcal{T}. \quad (4)$$

Second, it allows us to express the mole-fraction field as a linear combination of the structured component of $Y_1(\cdot, \cdot)$ and the flux dimension-reduction error component, as we now show. Substituting (1) into (4), we have that

$$Y_2(\mathbf{s}, h, t) = Y_2^0(\mathbf{s}, h, t) + \sum_{j=1}^r \hat{\psi}_j(\mathbf{s}, h, t) \alpha_j + v_{2,1}(\mathbf{s}, h, t) + v_2(\mathbf{s}, h, t), \quad \mathbf{s} \in \mathbb{S}^2, h \in \mathbb{R}^+, t \in \mathcal{T}, \quad (5)$$

where $Y_2^0(\mathbf{s}, h, t) \equiv \hat{\mathcal{H}}(\hat{Y}_2(\cdot, \cdot, t_0), 0; \mathbf{s}, h, t) + \hat{\mathcal{H}}(0, Y_1^0(\cdot, \mathcal{T}_t); \mathbf{s}, h, t)$; $\hat{\psi}_j(\mathbf{s}, h, t) \equiv \hat{\mathcal{H}}(0, \phi_j(\cdot, \mathcal{T}_t); \mathbf{s}, h, t)$, $j = 1, \dots, r$, are basis functions in mole-fraction space, often termed *response functions* (e.g., Saeki et al., 2013); and $v_{2,1}(\mathbf{s}, h, t) \equiv \hat{\mathcal{H}}(0, v_1(\cdot, \mathcal{T}_t); \mathbf{s}, h, t)$ is the impact of flux dimension-reduction error on the mole fraction at (\mathbf{s}, h, t) after application of the approximate transport model $\hat{\mathcal{H}}$; and $v_2(\mathbf{s}, h, t)$ is the residual term given in (3). We assume that $\text{E}(v_2(\cdot, \cdot, \cdot)) = 0$; in this case $Y_2^0(\mathbf{s}, h, t)$, can be seen as the prior expectation of the mole-fraction field at (\mathbf{s}, h, t) under $\hat{\mathcal{H}}$ and $\hat{Y}_2(\cdot, \cdot, t_0)$. That is, it is the mole fraction field generated by running our CTM with the input fluxes set to the prior expected flux, and with the mole-fraction field at t_0 set to $\hat{Y}_2(\cdot, \cdot, t_0)$.

Without further knowledge, the two spatio-temporal error processes $v_{2,1}(\cdot, \cdot, \cdot)$ and $v_2(\cdot, \cdot, \cdot)$ cannot be disentangled, and hence we do not attempt to model them separately. In Section 2.3 we will introduce another source of correlated error, and ultimately all these components are modelled together as one ‘model–data discrepancy’ term.

2.3 The mole-fraction data model

Fluxes cannot be observed directly at the spatial and temporal scales of interest. Flux inversion therefore proceeds by ‘constraining’ the flux field using column-averaged retrievals or point-referenced measurements of mole fraction. We use $Z_{2,i}$ to denote the i th mole-fraction measurement or retrieval, where $i \in \{1, \dots, m\}$ indexes the datum used in the inversion, and m is the number of data used in the inversion.

Point-referenced (PR) measurements of mole fraction are generally made at or near Earth’s surface, using instruments on towers or in aircraft. The mole-fraction data model for these measurements is therefore given by

$$Z_{2,i} = Y_2(\mathbf{s}_i, h_i, t_i) + \epsilon_i, \quad \text{if } Z_{2,i} \text{ is from a point-referenced instrument}, \quad (6)$$

where $Z_{2,i}$ is the observed mole fraction at (\mathbf{s}_i, h_i, t_i) , and ϵ_i is mean-zero Gaussian measurement error with

a model for its variance parameter presented below in Section 2.4. Measurement errors associated with point-referenced instruments are generally small and (usually) not correlated in space and time. Despite this, such data are not immune to the effects of spatio-temporal correlations induced by the CTM in the process model, and they may even be more susceptible than column-averaged retrievals due to the combined effect of their usual proximity to the surface and the discretisations employed when simulating approximate transport (Rayner and O’Brien, 2001; Basu et al., 2018).

Column-averaged (CA) retrievals, such as XCO₂ (where ‘X’ refers to the column averaged nature of the retrievals) from the Orbiting Carbon Observatory-2 (OCO-2) or the Total Carbon Column Observing Network (TCCON), are noisier than PR measurements, although TCCON less so. In particular, since the raw spectral information collected for the retrieval is affected by environmental factors such as aerosols (O’Dell et al., 2012), the errors can contain biases as well as exhibit spatio-temporal correlations. These biases can also be instrument-mode dependent (e.g., land glint vs land nadir retrievals; see Section 4.4.1). The vertical averaging operation also involves an averaging kernel and an *a priori* bias correction, which are both specific to the retrieval, and which arise from the algorithm used for the retrieval. In general, this relationship can be expressed as

$$Z_{2,i} = \hat{\mathcal{A}}_i(Y_2(\mathbf{s}_i, \cdot, t_i)) + b_i + v_{Z_{2,i}} + \epsilon_i, \quad \text{if } Z_{2,i} \text{ is a column-averaged retrieval,} \quad (7)$$

where (\mathbf{s}_i, t_i) is the space-time location of the retrieval, $\hat{\mathcal{A}}_i$ is the assumed (but necessarily approximate) observation operator of the i th retrieval that column-averages the mole fraction field via an averaging kernel; b_i is bias; $v_{Z_{2,i}}$ is mean-zero spatio-temporally correlated random error; and ϵ_i is mean-zero uncorrelated random error. The bias and error terms arise from the use of an approximate observation operator. Surface-based or remotely sensed CA retrievals are sometimes provided as ‘bias-corrected.’ In this case, the data model for these retrievals is identical to (7) but with the bias component omitted.

Substituting (5) into (6) and (7) we see that, in general, we have that

$$Z_{2,i} = \hat{Z}_{2,i}^0 + \sum_{j=1}^r \hat{\psi}_{j,i} \alpha_j + b_i + \xi_i + \epsilon_i, \quad (8)$$

where, for a PR measurement, $\hat{Z}_{2,i}^0 \equiv Y_2^0(\mathbf{s}_i, h_i, t_i)$; $\hat{\psi}_{j,i} \equiv \hat{\psi}_j(\mathbf{s}_i, h_i, t_i)$; $b_i = 0$; and $\xi_i \equiv v_{2,1}(\mathbf{s}_i, h_i, t_i) + v_2(\mathbf{s}_i, h_i, t_i)$; while for a CA retrieval, $\hat{Z}_{2,i}^0 \equiv \hat{\mathcal{A}}_i(Y_2^0(\mathbf{s}_i, \cdot, t_i))$; $\hat{\psi}_{j,i} \equiv \hat{\mathcal{A}}_i(\hat{\psi}_j(\mathbf{s}_i, \cdot, t_i))$, $j = 1, \dots, r$; and $\xi_i \equiv \hat{\mathcal{A}}_i(v_{2,1}(\mathbf{s}_i, \cdot, t_i) + v_2(\mathbf{s}_i, \cdot, t_i)) + v_{Z_{2,i}}$. Bias-corrected retrievals follow (8) but with the bias component omitted. Note that, for identifiability reasons, we have modelled all the various correlated-error terms using one component, $\{\xi_i\}$.

Flux inversions can make use of both PR measurements and CA retrievals simultaneously, and hence it is convenient to provide a data model that encapsulates both types of measurements. It is also often the case that measurements from the same instrument type can be divided into groups that can be expected to have similar characteristics, such as group-specific bias and error properties. A given group could contain, for example, PR data from the same *in situ* instrument, or CA retrievals from a particular remote sensing instrument under a specific retrieval mode (e.g., land nadir). Hence, we consider the following general data model, where different groups have different terms, but the overall structure is the same:

$$\mathbf{Z}_{2,g} = \hat{\mathbf{Z}}_{2,g}^0 + \hat{\mathbf{\Psi}}_g \boldsymbol{\alpha} + \mathbf{b}_g + \boldsymbol{\xi}_g + \boldsymbol{\epsilon}_g, \quad g = 1, \dots, n_g, \quad (9)$$

where n_g is the number of groups; $\mathbf{Z}_{2,g}$ contains the data in group g ; $\hat{\mathbf{Z}}_{2,g}^0$ are the prior expected mole-fractions under the approximate transport model and, if the groups consist of CA retrievals, under the approximate observation operators; $\hat{\mathbf{\Psi}}_g$ are the response functions evaluated at either the PR locations (in the case of PR measurements) or averaged over a column via an approximate observation operator (in the case of CA retrievals); $\mathbf{b}_g \equiv \mathbf{A}_g \boldsymbol{\beta}_g$ are group-specific biases, with \mathbf{A}_g a group-specific design matrix and $\boldsymbol{\beta}_g$ the corresponding weights; $\boldsymbol{\xi}_g$ is the group’s vector of correlated errors; and $\boldsymbol{\epsilon}_g$ is the group’s vector of uncorrelated errors. When the data in the group are considered to be unbiased (or already bias-corrected), the term $\mathbf{A}_g \boldsymbol{\beta}_g = \mathbf{0}$. The variables constituting $\boldsymbol{\beta}_g$ and $\boldsymbol{\epsilon}_g$, for $g = 1, \dots, n_g$, are mutually independent within and across groups.

The most difficult terms to characterise, and hence those most likely to lead to model misspecification issues, are the correlated error terms $\{\xi_g : g = 1, \dots, n_g\}$, since these are sums of multiple unidentifiable error terms. Clearly, $\{\xi_g\}$ are correlated both within and between groups, as they have common sources of variation such as transport-model error. However, our Bayesian statistical framework in WOMBAT assumes that $\{\xi_g\}$ are independent across groups, for two reasons. The first reason is computational, as estimating cross-correlations between groups adds an extra layer of computational complexity that is probably unnecessary given the amount of data that can be expected within each group. The second reason is more subtle and relates to covariance nonstationarity in the transport model and the flux dimension-reduction error. This covariance nonstationarity manifests itself as nonstationarity in the correlation of the model–data discrepancy, and the simplest way to model this effect is to assume independence across groups of measurements that are proximal in space and/or time (such as measurements from the same *in situ* instrument) and then to fit separate covariance-model parameters to data from each group.

Irrespective of the model chosen for inter-group correlations, as demonstrated through its construction, the correlation between elements within each $\{\xi_g\}$ associated with measurements that are proximal in space and time are stronger than those that are farther apart. The elements will almost certainly also have substantial variance. However, there has been extensive discussion as to whether this correlation needs to be explicitly modelled within an inversion framework. While spatio-temporal correlation in model–data discrepancies is widely acknowledged (Chevallier, 2007; Ciais et al., 2010; Mukherjee et al., 2011; Miller et al., 2020), the general consensus is that using just the variance of ξ_g to add to the variance of the uncorrelated component (or, similarly, to omit this term entirely and just scale the variance of the ϵ_g instead), is sufficient (e.g., Michalak et al., 2005; Basu et al., 2013; Deng et al., 2016). However, as we show in simulations given in Section 5.1, even when a measurement-error variance inflation factor is estimated, statistical efficiency is lost under the assumption of uncorrelated errors if the errors truly are correlated. The main reason not to routinely model spatio-temporal correlations in global flux inversion appears to be computational; we discuss a way to rectify this bottleneck in Section 3. More details on how we represent the model–data discrepancy are given in Section 2.4.

2.4 The parameter model

The parameter model (i.e., prior distributions) is dependent on the specification of the flux process model, the mole-fraction process model, and the mole-fraction data model. Here, we describe the parameter model we use in the OSSE and in the MIP comparison in Section 5.

Parameters of the flux process model: In the experiments of Section 5, our flux basis functions are from bottom-up inventories that are divided into r_s spatial regions and r_t time spans. This construction yields $r = r_s \times r_t$ basis functions, and naturally suggests a temporal partitioning of α into $(\alpha_1, \dots, \alpha_{r_t})'$, where each $\alpha_k \in \mathbb{R}^{r_s}, k = 1, \dots, r_t$. This, in turn, suggests that a suitable model for α is the vector-autoregressive process, similar to that used by Peters et al. (2005) and Dahlén et al. (2020),

$$\alpha_{k+1} = \mathbf{M}(\boldsymbol{\kappa})\alpha_k + \mathbf{w}_k; \quad k = 1, \dots, r_t,$$

where, in our examples, we constrain the matrix $\mathbf{M}(\boldsymbol{\kappa})$ to be diagonal with non-zero elements equal to $\boldsymbol{\kappa} \equiv (\kappa_1, \dots, \kappa_{r_s})'$; and we let $\mathbf{w}_k \sim \text{Gau}(\mathbf{0}, \boldsymbol{\Sigma}_w)$, where the precision matrix $\mathbf{Q}_w \equiv \boldsymbol{\Sigma}_w^{-1}$ is diagonal with positive elements $\boldsymbol{\tau}_w \equiv (\tau_{w,j} : j = 1, \dots, r_s)'$. The flux-process parameters are therefore $\boldsymbol{\theta}_\alpha \equiv (\boldsymbol{\kappa}', \boldsymbol{\tau}_w)'$, which in turn govern the covariance matrix of α , $\boldsymbol{\Sigma}_\alpha \equiv \text{var}(\alpha)$. There is an ordering of α for which $\boldsymbol{\Sigma}_\alpha^{-1}$ is block-tridiagonal (see Appendix A). Either sequential estimation (e.g., Kalman filtering/smoothing) or batch Bayesian updating can be used to make inference on α . In our case we use the latter, and take advantage of efficient algorithms that are available for sparse linear algebraic computations.

We expect that $\{\alpha_k\}$ are positively correlated in time. Therefore, for the prior distributions for $\{\kappa_j : j = 1, \dots, r_s\}$, we use the Beta distribution: Independently,

$$\kappa_j \sim \text{Beta}(a_{\kappa,j}, b_{\kappa,j}), \quad j = 1, \dots, r_s,$$

where $\{a_{\kappa,j}\}$ and $\{b_{\kappa,j}\}$ are fixed and assumed known. For prior distributions for the precision parameters $\{\tau_{w,j}\}$ we use gamma distributions with shape parameters $\{\nu_{w,j}\}$ and rate parameters $\{\omega_{w,j}\}$, which are

fixed and assumed known: Independently,

$$\tau_{w,j} \sim \text{Ga}(\nu_{w,j}, \omega_{w,j}), \quad j = 1, \dots, r_s.$$

Michalak et al. (2005) suggested that variance parameters could be estimated directly in a maximum likelihood framework. The use of prior distributions on τ_w and κ adds an extra level of flexibility and allows the modeller to express the ‘uncertainty on the uncertainties’ in an inversion framework (e.g., Ganesan et al., 2014). One can configure these prior distributions to be extremely informative and, effectively, fix the prior model for the flux, or else make them extremely uninformative so that the posterior maximum-*a-posteriori* (MAP) estimates of the parameters in the prior flux-process model converge to the maximum likelihood estimates. This choice can be made on a region-by-region basis, as is the case in Section 4.5, where land regions are given uninformative priors and ocean regions are given informative ones.

CA mole-fraction retrieval bias parameters: In our studies of Section 5, we consider OCO-2 retrievals and a different set of bias parameters for each instrument mode. In this context, β_g is associated with a particular instrument mode and a single element of β_g captures the bias arising from, for example, aerosol presence. Investigations in Section 5.3 reveal that these bias parameters are quite easily constrained in an inversion framework. When constructing the model for each β_g , we first standardise each row in \mathbf{A}_g so that the covariates have unit marginal empirical variance. Then we model $\{\beta_g\}$ as follows: Independently,

$$\beta_g \sim \text{Gau}(\mathbf{0}, \sigma_\beta^2 \mathbf{I}), \quad g = 1, \dots, n_g,$$

with $\sigma_\beta^2 = 100$. This choice for σ_β^2 renders the prior distribution uninformative for the data-set sizes we consider in our experiments.

Model–data discrepancy and measurement-error parameters: For each $g = 1, \dots, n_g$, the terms ξ_g and ϵ_g need to be considered together, since often they are confounded in inversion studies. In particular, there are two cases we need to cater for:

Case (i): Measurements $\mathbf{Z}_{2,g}$ are usually provided to the modeller with accompanying uncertainty measures in the form of marginal standard errors. In this first case, the prescribed standard error is what we attribute to the component ϵ_g by constructing the (diagonal) covariance matrix, $\text{var}(\epsilon_g) \equiv \Sigma_{\epsilon,g}$, with the squared prescribed standard errors on the diagonal. However, it is likely that the prescribed standard errors are either over-estimates or under-estimates of the true standard error (Worden et al., 2017), and we therefore let $\text{diag}(\Sigma_{\epsilon,g}) = \gamma_g \cdot \mathbf{v}_g^{\text{ps}}$, where \mathbf{v}_g^{ps} is a vector containing the square of the prescribed standard errors, and $\{\gamma_g : g = 1, \dots, n_g\}$ are group-specific *inflation factors* (e.g., Michalak et al., 2005). We model the inflation factors using inverse-gamma distributions: Independently,

$$\gamma_g \sim \text{IG}(\nu_{\gamma_g}, \omega_{\gamma_g}), \quad g = 1, \dots, n_g,$$

where the shape and rate parameters, $\{\nu_{\gamma_g}\}$ and $\{\omega_{\gamma_g}\}$, are fixed and assumed known.

We model the covariance matrix $\Sigma_{\xi_g} \equiv \text{var}(\xi_g)$, using a spatio-temporal covariance function $C_{\xi_g}(\cdot, \cdot; \theta_{\xi_g})$ (e.g., Cressie and Wikle, 2011, Chapter 6), where the parameter vector θ_{ξ_g} contains unknown parameters that need to be inferred from the data. Here we have n_{τ_g} precision parameters, τ_{ξ_g} , and n_{ℓ_g} length scale parameters, ℓ_g ; that is, for Case (i), $\theta_{\xi_g} = (\tau_{\xi_g}', \ell_g')'$. We model each precision parameter and each length-scale parameter in each group using gamma distributions: Independently,

$$\begin{aligned} \tau_{\xi_g,j} &\sim \text{Ga}(\nu_{\xi_g,j}, \omega_{\xi_g,j}), \quad j = 1, \dots, n_{\tau_g}; \quad g = 1, \dots, n_g, \\ \ell_{g,j} &\sim \text{Ga}(\nu_{\ell_g,j}, \omega_{\ell_g,j}), \quad j = 1, \dots, n_{\ell_g}; \quad g = 1, \dots, n_g, \end{aligned}$$

where the shape and rate parameters $\{\nu_{\xi_g,j}\}$, $\{\omega_{\xi_g,j}\}$, $\{\nu_{\ell_g,j}\}$, and $\{\omega_{\ell_g,j}\}$, are fixed and assumed known.

Case (ii): Occasionally, as in the MIP of Crowell et al. (2019), one is provided with a measure of uncertainty that contains a component intended to account for CTM error. In this case, it is reasonable to let the *total marginal variance* from ξ_g and ϵ_g equal the inflated prescribed variance, $\gamma_g \cdot \mathbf{v}_g^{\text{ps}}$. We enforce this constraint by letting $\text{diag}(\Sigma_{\xi_g}) = \rho_g \gamma_g \cdot \mathbf{v}_g^{\text{ps}}$, and $\text{diag}(\Sigma_{\epsilon_g}) = (1 - \rho_g) \gamma_g \cdot \mathbf{v}_g^{\text{ps}}$. This formulation encapsulates the notion that the prescribed error includes the transport model–error component, but that the overall

contribution of that component is uncertain. Thus, the parameter ρ_g needs to be estimated in order to obtain the relative contribution of the correlated component. The inflation factor γ_g is still needed since, first, the prescribed variances could still be misspecified and, second, even if the prescribed variances were correctly specified, they do not take into account the dimension-reduction error, that is specific to the flux process model.

We model the contribution factors $\{\rho_g : g = 1, \dots, n_g\}$ via a standard uniform distribution: Independently,

$$\rho_g \sim \text{Unif}(0, 1), \quad g = 1, \dots, n_g,$$

and, as in Case (i), we use gamma prior distributions to model the length scales $\{\ell_g\}$ in the covariance function. For Case (ii), $\boldsymbol{\theta}_{\xi_g} = (\rho_g, \boldsymbol{\ell}'_g)'$.

2.5 Summary of the Bayesian model and computation

To summarise, the Bayesian model we implement in WOMBAT consists of a flux process model, a mole-fraction process model, a mole-fraction data model, and a parameter model, where the parameter model depends on the specifications of the other three. The hierarchical Bayesian model, which we use in the examples of Section 5, can be written succinctly as follows: Independently,

Flux scaling factors autoregressive parameters:	$\kappa_j \sim \text{Beta}(a_{\kappa,j}, b_{\kappa,j}), \quad j = 1, \dots, r_s,$
Flux scaling factors innovation-term precisions:	$\tau_{w,j} \sim \text{Ga}(\nu_{w,j}, \omega_{w,j}), \quad j = 1, \dots, r_s,$
Flux scaling factors:	$\boldsymbol{\alpha} \mid \boldsymbol{\kappa}, \boldsymbol{\tau}_w \sim \text{Gau}(\mathbf{0}, \boldsymbol{\Sigma}_\alpha),$
Measurement-bias coefficients:	$\boldsymbol{\beta}_g \sim \text{Gau}(\mathbf{0}, \sigma_\beta^2 \mathbf{I}), \quad g = 1, \dots, n_g,$
Measurement-error variance inflation factors:	$\gamma_g \sim \text{IG}(\nu_{\gamma_g}, \omega_{\gamma_g}), \quad g = 1, \dots, n_g,$
Correlated-error length scales:	$\ell_{g,j} \sim \text{Ga}(\nu_{\ell_{g,j}}, \omega_{\ell_{g,j}}), \quad j = 1, \dots, n_{\ell_g}; \quad g = 1, \dots, n_g,$
Correlated-error precisions (only Case (i)):	$\tau_{\xi_{g,j}} \sim \text{Ga}(\nu_{\xi_{g,j}}, \omega_{\xi_{g,j}}), \quad j = 1, \dots, n_{\tau_g}; \quad g = 1, \dots, n_g,$
Correlated-error contribution (only Case (ii)):	$\rho_g \sim \text{Unif}(0, 1), \quad g = 1, \dots, n_g,$
Likelihood:	$\mathbf{Z}_2 \mid \boldsymbol{\beta}, \boldsymbol{\alpha}, \boldsymbol{\theta}_{\xi,\epsilon} \sim \text{Gau}(\hat{\mathbf{Z}}_2^0 + \hat{\boldsymbol{\Psi}}\boldsymbol{\alpha} + \mathbf{A}\boldsymbol{\beta}, \boldsymbol{\Sigma}_\xi + \boldsymbol{\Sigma}_\epsilon),$

where $\mathbf{Z}_2 \equiv (\mathbf{Z}'_{2,1}, \dots, \mathbf{Z}'_{2,n_g})'$, $\hat{\mathbf{Z}}_2^0 \equiv (\hat{\mathbf{Z}}_{2,1}^0, \dots, \hat{\mathbf{Z}}_{2,n_g}^0)'$, $\hat{\boldsymbol{\Psi}} \equiv (\hat{\boldsymbol{\Psi}}'_1, \dots, \hat{\boldsymbol{\Psi}}'_{n_g})'$, $\mathbf{A} \equiv \text{bdiag}(\mathbf{A}_1, \dots, \mathbf{A}_{n_g})$, $\boldsymbol{\beta} \equiv (\boldsymbol{\beta}'_1, \dots, \boldsymbol{\beta}'_{n_g})'$, $\boldsymbol{\Sigma}_\xi \equiv \text{bdiag}(\boldsymbol{\Sigma}_{\xi_1}, \dots, \boldsymbol{\Sigma}_{\xi_{n_g}})$, $\boldsymbol{\Sigma}_\epsilon \equiv \text{bdiag}(\boldsymbol{\Sigma}_{\epsilon_1}, \dots, \boldsymbol{\Sigma}_{\epsilon_{n_g}})$, and $\boldsymbol{\theta}_{\xi,\epsilon} \equiv ((\boldsymbol{\theta}'_{\xi_g}, \gamma_g) : g = 1, \dots, n_g)'$. Here, $\text{bdiag}(\cdot)$ constructs a block-diagonal matrix from its arguments. A graphical model summarising the relationships between the variables is given in Figure 1.

The joint posterior distribution over all quantities can be estimated using a Gibbs sampler, which successively ‘updates’ parameters using their full conditional distributions. Often, our choice of prior distributions ensure that these conditional distributions are of known form and can be sampled from directly. When this is not the case (in particular, for the parameters $\boldsymbol{\kappa}$, $\boldsymbol{\ell}_g$, and ρ_g , where $g = 1, \dots, n_g$), we employ a slice sampler (Neal, 2003) to obtain samples from the full conditional distributions. Details are given in Appendix A.

3 Markov assumptions on the model–data discrepancy

The posterior distribution over all the unknown parameters in our model is given by

$$p(\boldsymbol{\alpha}, \boldsymbol{\beta}, \boldsymbol{\kappa}, \boldsymbol{\tau}_w, \boldsymbol{\theta}_{\xi,\epsilon} \mid \mathbf{Z}_2) \propto p(\mathbf{Z}_2 \mid \boldsymbol{\beta}, \boldsymbol{\alpha}, \boldsymbol{\theta}_{\xi,\epsilon}) p(\boldsymbol{\alpha} \mid \boldsymbol{\kappa}, \boldsymbol{\tau}_w) p(\boldsymbol{\beta}) p(\boldsymbol{\theta}_{\xi,\epsilon}) p(\boldsymbol{\kappa}) p(\boldsymbol{\tau}_w). \quad (10)$$

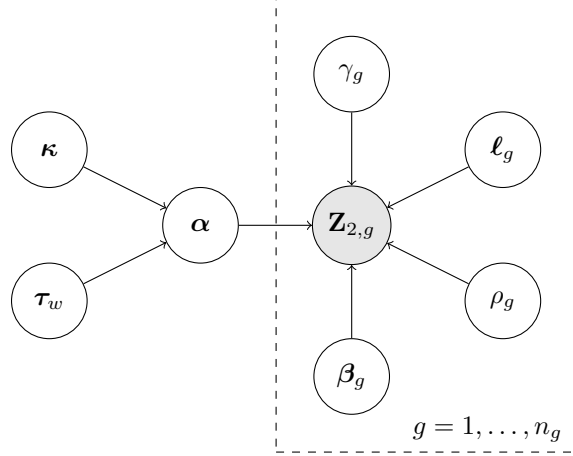


Fig. 1: Graphical model summarising the relationship between the variables and parameters to be inferred and the grouped data $\{\mathbf{Z}_{2,g} : g = 1, \dots, n_g\}$ in Case (ii). In Case (i) we replace ρ_g with τ_{ξ_g} .

The log of the first two terms on the right-hand side of (10) are expressions that are commonly seen in optimisation-based flux-inversion frameworks. In particular, we have that

$$\begin{aligned} \log p(\mathbf{Z}_2 | \boldsymbol{\beta}, \boldsymbol{\alpha}, \boldsymbol{\theta}) p(\boldsymbol{\alpha} | \boldsymbol{\kappa}, \boldsymbol{\theta}_w) &= -\frac{1}{2} \log |\boldsymbol{\Sigma}_\xi + \boldsymbol{\Sigma}_\epsilon| - \frac{1}{2} (\mathbf{Z}_2 - \mathbf{Z}_{2,p}(\boldsymbol{\beta}, \boldsymbol{\alpha}))' (\boldsymbol{\Sigma}_\xi + \boldsymbol{\Sigma}_\epsilon)^{-1} (\mathbf{Z}_2 - \mathbf{Z}_{2,p}(\boldsymbol{\beta}, \boldsymbol{\alpha})) \\ &\quad - \frac{1}{2} \log |\boldsymbol{\Sigma}_\alpha| - \frac{1}{2} (\boldsymbol{\alpha} - \boldsymbol{\alpha}_p)' \boldsymbol{\Sigma}_\alpha^{-1} (\boldsymbol{\alpha} - \boldsymbol{\alpha}_p) + \text{const.}, \end{aligned} \quad (11)$$

where $\mathbf{Z}_{2,p}(\boldsymbol{\beta}, \boldsymbol{\alpha}) \equiv \hat{\mathbf{Z}}_2^0 + \hat{\boldsymbol{\Psi}}\boldsymbol{\alpha} + \mathbf{A}\boldsymbol{\beta}$, in our case we set $\boldsymbol{\alpha}_p = \mathbf{0}$, and “const.” denotes a constant. The primary differences to popular optimisation-based flux-inversion frameworks are the presence of the log-determinants, which penalise covariance matrices that have large determinants (large correlations and/or large variances), and the presence of off-diagonal elements in the matrix $\boldsymbol{\Sigma}_\xi + \boldsymbol{\Sigma}_\epsilon$. The log-determinants can only be omitted when all covariance matrices are considered known *a priori*.

The computational complexity of the Gibbs sampler is dominated by that of the log-likelihood function $\log p(\mathbf{Z}_2 | \boldsymbol{\beta}, \boldsymbol{\alpha}, \boldsymbol{\theta}_{\xi, \epsilon})$, which is the sum of the group-wise log-likelihood functions, $\log p(\mathbf{Z}_{2,g} | \boldsymbol{\beta}, \boldsymbol{\alpha}, \boldsymbol{\theta}_{\xi, \epsilon})$, $g = 1, \dots, n_g$. For computationally efficient inference, we must hence ensure that each group-wise log-likelihood function is simple to evaluate. From (9), the group-wise log-likelihood is given by

$$\log p(\mathbf{Z}_{2,g} | \boldsymbol{\beta}, \boldsymbol{\alpha}, \boldsymbol{\theta}_{\xi, \epsilon}) = -\frac{m_g}{2} \log 2\pi - \frac{1}{2} \log |\boldsymbol{\Sigma}_g| - \frac{1}{2} (\mathbf{Z}_{2,g} - \hat{\mathbf{Z}}_{2,g}^0 - \hat{\boldsymbol{\Psi}}_g \boldsymbol{\alpha} - \mathbf{A}_g \boldsymbol{\beta}_g)' \boldsymbol{\Sigma}_g^{-1} (\mathbf{Z}_{2,g} - \hat{\mathbf{Z}}_{2,g}^0 - \hat{\boldsymbol{\Psi}}_g \boldsymbol{\alpha} - \mathbf{A}_g \boldsymbol{\beta}_g), \quad (12)$$

for $g = 1, \dots, n_g$, where $\boldsymbol{\Sigma}_g \equiv \boldsymbol{\Sigma}_{\xi_g} + \boldsymbol{\Sigma}_{\epsilon_g}$, and m_g is the number of data in group g . From a computational perspective there are two components in (12) that can present difficulties. The first component is the matrix $\hat{\boldsymbol{\Psi}}_g$; this matrix is dense, and its number of elements scales linearly with both the number of data points and the number of basis functions, r . However, this matrix just needs to be evaluated once using the CTM and can typically be generated efficiently on a large parallel computing infrastructure (see Section 4.6). The second component is the matrix $\boldsymbol{\Sigma}_g$, which is of size $m_g \times m_g$ and generally dense. Recall from Section 2.4 that this covariance matrix is constructed using a spatio-temporal covariance function $C_{\xi_g}(\cdot, \cdot; \boldsymbol{\theta}_{\xi_g})$, where the parameters $\boldsymbol{\theta}_{\xi_g}$ are sampled within the Gibbs sampler. Therefore, this covariance matrix needs to be re-constructed at each sampler iteration. For $m_g \approx 100,000$, as in this study, the dense matrix $\boldsymbol{\Sigma}_g$ is too large to fit in the random-access memory of most computers, let alone factorised, which is infeasible.

We deal with $\boldsymbol{\Sigma}_g$ by using an approximation first proposed by Vecchia (1988), and further formalised under the guise of nearest-neighbour Gaussian processes by Datta et al. (2016). Here, one first orders the

elements of $\boldsymbol{\xi}_g$. Then, one approximates the joint distribution of $\boldsymbol{\xi}_g$ as,

$$p(\boldsymbol{\xi}_g) = p(\xi_{g,1}) \prod_{i=2}^{m_g} p(\xi_{g,i} \mid \boldsymbol{\xi}_{g,1:(i-1)}) \approx p(\xi_{g,1}) \prod_{i=2}^{m_g} p(\xi_{g,i} \mid \boldsymbol{\xi}_{g,\mathcal{N}_{g,i}}), \quad (13)$$

where $\mathcal{N}_{g,i}$ is the ‘‘past’’ neighbour set of the i th datum in group g , which contains a (very small) subset of the integers between, and including, 1 and $(i - 1)$. It can be shown that this formulation leads to a valid distribution for $\boldsymbol{\xi}_g$ that approximates the true joint distribution. The approximate distribution is Gaussian with mean $\mathbf{0}$ and a sparse precision matrix, $\boldsymbol{\Sigma}_{\xi,g}^{-1}$, with the degree of sparsity closely connected to the sizes of the sets $\{\mathcal{N}_{g,i} : i = 1, \dots, m_g\}$.

In the version of WOMBAT presented here, we consider a special case of (13), where the observations are ordered in time and where the covariance function $C_{\xi_g}(\cdot, \cdot; \boldsymbol{\theta}_{\xi_g})$ is simply an exponential function of temporal separation. In this case one only needs the consideration of one (temporal) length-scale parameter per group, $\ell_{g,1}, g = 1, \dots, n_g$. The motivations for this simplification are twofold. First, the remote-sensing instrument we consider in Sections 4 and 5 flies on a satellite that is in a sun-synchronous orbit, so that correlation in time is a proxy for along-track correlations. This model for characterising correlation in the errors was suggested and used by Chevallier (2007). Second, the use of an exponential covariance function allows the approximation in (13) to become an equality, where $\mathcal{N}_{g,i} = i - 1$. This is a manifestation of the so-called ‘screening effect,’ where the exponential covariance function induces a first-order conditional independence structure. Consequently, $\boldsymbol{\Sigma}_{\xi_g}^{-1}$ is a tridiagonal matrix of known form; a similar structure was proposed by Lunt et al. (2016) for *in situ* measurements in a regional inversion for methane fluxes. Denote the (temporally ordered) measurement times within a group as t_1, t_2, \dots, t_{m_g} , the normalised temporal separations as $\delta_k \equiv (t_{k+1} - t_k)/\ell_{g,1}$, for $k = 1, \dots, m_g - 1$, and the marginal variances of $\boldsymbol{\xi}_g$ as $\sigma_{\xi_g,k}^2$, for $k = 1, \dots, m_g$. Then, it can be shown (e.g., Finley et al., 2009) that $\boldsymbol{\Sigma}_{\xi_g}^{-1}$ has diagonal entries $\sigma_{\xi_g,k}^{-2} d_{\xi_g,k}$, for $k = 1, \dots, m_g$, where

$$d_{\xi_g,k} = \begin{cases} 1 + \frac{e^{-2\delta_1}}{1 - e^{-2\delta_1}} & \text{if } k = 1, \\ 1 + \frac{e^{-2\delta_k}}{1 - e^{-2\delta_k}} + \frac{e^{-2\delta_{k+1}}}{1 - e^{-2\delta_{k+1}}} & \text{if } k = 2, 3, \dots, m_g - 1, \\ 1 + \frac{e^{-2\delta_{m_g}}}{1 - e^{-2\delta_{m_g}}} & \text{if } k = m_g, \end{cases}$$

and sub-diagonal entries $\sigma_{\xi_g,k}^{-1} \sigma_{\xi_g,k+1}^{-1} s_{\xi_g,k}$, for $k = 1, \dots, m_g - 1$, where

$$s_{\xi_g,k} = -\frac{e^{-\delta_k}}{1 - e^{-2\delta_k}}.$$

Now, $\boldsymbol{\Sigma}_g^{-1} = (\boldsymbol{\Sigma}_{\xi_g} + \boldsymbol{\Sigma}_{\epsilon_g})^{-1}$ and $|\boldsymbol{\Sigma}_g| = |\boldsymbol{\Sigma}_{\xi_g} + \boldsymbol{\Sigma}_{\epsilon_g}|$, where $\boldsymbol{\Sigma}_{\xi_g}^{-1}$ is very sparse and $\boldsymbol{\Sigma}_{\epsilon_g}^{-1}$ is diagonal. Efficient computations of (12) therefore follows by expressing $\boldsymbol{\Sigma}_g^{-1}$ and $|\boldsymbol{\Sigma}_g|$ in terms of these sparse matrices. Then $\boldsymbol{\Sigma}_g^{-1}$ and $|\boldsymbol{\Sigma}_g|$ can be evaluated through the use of the Sherman–Morrison–Woodbury matrix identity and a matrix-determinant lemma (e.g., Henderson and Searle, 1981, and Appendix A).

4 Setup of flux-inversion framework

This section gives the setup needed for Section 5, where we compare the inversions from WOMBAT to those from the OCO-2 MIP (Crowell et al., 2019). In the MIP, inversions followed a predefined protocol; we therefore configured WOMBAT to follow the same protocol. The MIP prescribed the data to be used, including both preprocessed point referenced and remotely sensed data from OCO-2 between 06 September 2014 and 01 April 2017. Participants were tasked to provide flux estimates for the years 2015 and 2016. The protocol also specified a fossil-fuel flux field that had to be assumed fixed and known, in order to facilitate the interpretation of the differences in flux estimates obtained by the different participants. All other modelling

choices (e.g., transport model, prior fluxes) were left to individual participants.

4.1 Prior expected flux

Our prior expectation of the spatio-temporal flux process, $Y_1^0(\cdot, \cdot)$, is constructed from inventories of different types of fluxes through the decomposition

$$Y_1^0(\mathbf{s}, \cdot) = \begin{cases} Y_1^{0,\text{ff}}(\mathbf{s}, \cdot) + Y_1^{0,\text{bio}}(\mathbf{s}, \cdot) + Y_1^{0,\text{bf}}(\mathbf{s}, \cdot) + Y_1^{0,\text{fire}}(\mathbf{s}, \cdot), & \text{if } \mathbf{s} \text{ is over land,} \\ Y_1^{0,\text{ff}}(\mathbf{s}, \cdot) + Y_1^{0,\text{ocn}}(\mathbf{s}, \cdot), & \text{if } \mathbf{s} \text{ is over ocean,} \end{cases} \quad (14)$$

where $Y_1^{0,\text{ff}}(\cdot, \cdot)$ corresponds to fossil fuel emissions, $Y_1^{0,\text{bio}}(\cdot, \cdot)$ to terrestrial biospheric fluxes, $Y_1^{0,\text{bf}}(\cdot, \cdot)$ to biofuel emissions, $Y_1^{0,\text{fire}}(\cdot, \cdot)$ to fire emissions, and $Y_1^{0,\text{ocn}}(\cdot, \cdot)$ to ocean-air exchange fluxes. We now describe these components in more detail:

- Fossil-fuel emissions: For $Y_1^{0,\text{ff}}(\cdot, \cdot)$ we use the Open-source Data Inventory for Anthropogenic CO₂ monthly fossil-fuel emissions (ODIAC2016; Oda and Maksyutov, 2011; Oda et al., 2018) with Temporal Improvements for Modeling Emissions by Scaling (TIMES) weekly scaling factors (Nassar et al., 2013). This term also includes emissions from international aviation and shipping. The fossil-fuel fluxes are prescribed by the MIP protocol.
- Biospheric flux: This flux is a result of the interaction between the atmosphere and trees, shrubs, grasses, soils, dead wood, leaf litter, and other biota. It is defined by the formula $\text{GPP} - R_A - R_H$, where GPP stands for gross primary production and represents the uptake of carbon by plants due to photosynthesis; R_A is autotrophic respiration, the release of carbon through respiration by plants; and R_H is heterotrophic respiration, the release of carbon through the metabolic action of bacteria, fungi, and animals. For $Y_1^{0,\text{bio}}(\cdot, \cdot)$ we use one of the two priors used in CarbonTracker 2019 (Jacobson et al., 2020), specifically that based on the Carnegie-Ames Stanford Approach (CASA) biogeochemical model (Potter et al., 1993; Giglio et al., 2013).
- Biofuel emissions: These emissions result from the burning of wood, charcoal, and agricultural waste for energy, as well as the burning of agricultural fields. For $Y_1^{0,\text{bf}}(\cdot, \cdot)$ we use the estimates of Yevich and Logan (2003) that in turn were based on data from 1985.
- Fire emissions: These emissions correspond to those from vegetative fires (wildfires), which may start either naturally or by humans. For $Y_1^{0,\text{fire}}(\cdot, \cdot)$ we use the Quick Fire Emissions Dataset, version 2 (QFED2; Darmenov and da Silva, 2015).
- Ocean-air exchange: These fluxes are a result of ocean-air differences in partial pressure of CO₂. For $Y_1^{0,\text{ocn}}(\cdot, \cdot)$ we use the estimates of Takahashi et al. (2002), with annual scalings reflecting increasing uptake of CO₂ as described by Takahashi et al. (2009).

A summary of these components is provided in Table 1.

4.2 Basis functions

We divided the globe into the $r_s = 22$ disjoint TransCom3 regions (Gurney et al., 2002), and time into the $r_t = 31$ months between (and including) September 2014 and March 2017, and then we constructed one flux basis function for each region/month pair. This yielded $r = r_s \times r_t = 682$ basis functions, each with non-zero support in a space-time volume spanning one month in time, and one TransCom3 region in space. Half of the TransCom3 regions are land regions, and half are ocean regions, so that half of our basis functions correspond to land areas, and half to ocean areas. We show the TransCom3 regions in Figure C1, and their codes and labels in Table C1, both of which can be found in Appendix C. Some areas of the globe, depicted in white in Figure C1, are assumed to have zero flux; all our basis functions are zero in these regions.

Table 1: Components of the flux prior $Y_1^0(\mathbf{s}, t)$ used in (14).

Symbol	Type	Inventory name	Resolution	Reference(s)
$Y_1^{0,\text{ff}}(\cdot, \cdot)$	Fossil fuel	Open-source Data Inventory for Anthropogenic CO ₂ 2016 (ODIAC2016) & Temporal Improvements for Modeling Emissions by Scaling (TIMES)	Monthly + hourly scaling	Oda and Maksyutov (2011); Nassar et al. (2013); Oda et al. (2018)
$Y_1^{0,\text{bio}}(\cdot, \cdot)$	Biospheric	CarbonTracker 2019, based on the Carnegie-Ames Stanford Approach (CASA) biogeochemical model	3 hourly	Potter et al. (1993); Giglio et al. (2013); Jacobson et al. (2020)
$Y_1^{0,\text{bf}}(\cdot, \cdot)$	Biofuels	Yevich & Logan	Constant	Yevich and Logan (2003)
$Y_1^{0,\text{fire}}(\cdot, \cdot)$	Fires	Quick Fire Emissions Dataset, version 2 (QFED2)	Hourly	Darmenov and da Silva (2015)
$Y_1^{0,\text{ocn}}(\cdot, \cdot)$	Ocean	Scaled Takahashi	Monthly	Takahashi et al. (2002); Takahashi et al. (2009)

For $\phi_j(\cdot, \cdot)$ a basis function corresponding to a land area, we have

$$\phi_j(\mathbf{s}, t) = \begin{cases} Y_1^{0,\text{bio}}(\mathbf{s}, t) + Y_1^{0,\text{bf}}(\mathbf{s}, t) + Y_1^{0,\text{fire}}(\mathbf{s}, t), & (\mathbf{s}', t)' \in D_j^\phi, \\ 0 & \text{otherwise,} \end{cases} \quad (15)$$

where D_j^ϕ is the space-time volume over which the j th basis function is defined to be non-zero. For $\phi_j(\cdot, \cdot)$ a basis function corresponding to an ocean area, we have

$$\phi_j(\mathbf{s}, t) = \begin{cases} Y_1^{0,\text{ocn}}(\mathbf{s}, t), & (\mathbf{s}', t)' \in D_j^\phi, \\ 0 & \text{otherwise.} \end{cases} \quad (16)$$

Note that both (15) and (16) exclude $Y_1^{0,\text{ff}}(\cdot, \cdot)$. This is done to meet the MIP requirement that fossil-fuel fluxes are treated as fixed and known (which is common practice in flux inversion; e.g., see Basu et al., 2013). The influence of fossil fuels on the mole-fraction field is therefore present only as an invariant component of the prior expectation of the mole-fraction field.

Since the spatio-temporal patterns of the fluxes within a region-month space-time volume are fixed, our construction is quite restrictive. However, the space-time patterns are dictated by those in the inventories used to construct the basis functions, and they can be assumed to be fairly realistic. This underlying assumption is ubiquitous in flux-inversion systems; for example, Jacobson et al. (2020) scale 3-hourly fluxes using weekly scale factors over 156 regions, while Basu et al. (2013) use monthly scale factors for 3-hourly fluxes over $6^\circ \times 4^\circ$ grid cells. Constraining the spatio-temporal pattern is inferentially advantageous because it helps address the ill-posed nature of flux inversion. It is also computationally advantageous because it reduces the number of unknowns for which inference is needed. The disadvantage is that the reliance on *a priori* structures increases the risk of dimension-reduction error because, while our basis functions allow the posterior fluxes to vary at sub-TransCom3-region scales, variations that don't follow the prescribed pattern are necessarily ignored.

As described in Section 2.2, for $j = 1, \dots, 682$, each flux basis function $\phi_j(\cdot, \cdot)$ has a corresponding mole-

fraction basis function $\hat{\psi}_j(\cdot, \cdot, \cdot)$, which may be constructed by running the transport model, $\hat{\mathcal{H}}$, under the flux $Y_1^0(\cdot, \cdot) + \phi_j(\cdot, \cdot)$. Then the mole-fraction basis function $\hat{\psi}_j(\cdot, \cdot, \cdot)$ is recovered through linearity by simply subtracting $Y_2^0(\cdot, \cdot, \cdot)$ from the output mole-fraction field. For illustration, Figure 2 shows examples of the flux basis functions (monthly averaged) for January 2016 and the regions TransCom3 02 and TransCom3 06, and snapshots of the corresponding mole-fraction basis functions (daily and atmospheric-column averaged) obtained using the transport model described next in Section 4.3.

4.3 Transport model and initial condition

For our approximate transport model, $\hat{\mathcal{H}}$, we used the GEOS-Chem global 3-D chemical transport model, version 12.3.2 (Bey et al., 2001; Yantosca, 2019), driven by the GEOS-FP meteorological fields from NASA’s Goddard Earth Observing System (Rienecker et al., 2008). We use the offline GEOS-Chem CO₂ simulation (Nassar et al., 2010), with the native horizontal resolution of $0.25^\circ \times 0.3125^\circ$ and 72 vertical levels aggregated to $2^\circ \times 2.5^\circ$ and 47 vertical levels for computational efficiency. We use a transport time step of 10 minutes, and a flux time step of 20 minutes. All fluxes described in sections 4.1 and 4.2 were implemented in GEOS-Chem using the HEMCO emissions component (Keller et al., 2014). GEOS-Chem can be configured to allow for a 3-D chemical source of CO₂ due to oxidation of other trace gases, but this was disabled for compatibility with the OCO-2 MIP.

The approximate initial condition, $\hat{Y}_2(\cdot, \cdot, t_0)$, specifies the mole-fraction field at the beginning of the study period on 01 September 2014. For our initial mole-fraction field, we used a modified version of that generated by Bukosa et al. (2019). This mole-fraction field was constructed using a spin-up period, starting on 01 January 2005, and ending on 01 September 2014, with transport driven by inventory fluxes and meteorology (that in some cases differ from those we use here; see Bukosa et al., 2019, for details). At the end of the spin-up period, the whole mole-fraction field on 01 September 2014 was scaled such that the value in the surface grid cell containing the South Pole was equal to the monthly-averaged mole-fraction measurement from surface flask measurements at the South Pole (Thoning et al., 2020) in September 2014. The South Pole was chosen as our calibration point due its physical isolation from strong sources and sinks.

4.4 Data

This study uses a subset of the data sources in the MIP (Crowell et al., 2019). These include retrievals of column-averaged CO₂ by NASA’s OCO-2 satellite (Eldering et al., 2017), and retrievals of column-averaged CO₂ from TCCON (Wunch et al., 2011a). As in the MIP, we use OCO-2 data to estimate CO₂ fluxes, and TCCON data to validate the estimates.

4.4.1 OCO-2

The OCO-2 satellite was launched in 2014 with the goal of retrieving atmospheric CO₂ mole fractions. The on-board instrument measures radiances in three near-infrared spectral bands, which in turn are used to retrieve the CO₂ mole fraction on 20 vertical levels via a retrieval algorithm based on Bayesian optimal estimation (Rodgers, 2000; O’Dell et al., 2012). The retrieved levels are column-averaged, and then bias-corrected through comparison with TCCON retrievals (Wunch et al., 2011a). The OCO-2 team releases regular revisions of the retrieval dataset.

OCO-2 radiance measurements are taken in three distinct pointing modes: nadir mode, where the satellite aims at the point directly beneath it; glint mode, where the satellite points at the reflection of the sun on the surface; and target mode, where the satellite aims at a specific target, typically a ground station that also measures CO₂ mole fractions. Target observations are generally excluded from flux inversions and used only for instrument calibration. Over the ocean, nadir measurements have insufficient signal-to-noise ratio to provide useful retrievals, while over land, both nadir and glint retrievals are made. There are therefore three retrieval modes to consider, land glint (LG), land nadir (LN), and ocean glint (OG). The error properties of retrievals over land differ significantly from those over ocean; in particular, the OG retrievals in the V7r dataset (the dataset used in the MIP) are not considered reliable, and were therefore excluded from the MIP (Crowell et al., 2019). We follow this protocol, and only do inversions using LG and LN data.

The MIP protocol dictated the use of a post-processed version of the V7r retrievals; this post-processing was done as follows. First, an additional bias-correction term related to high-albedo measurements was

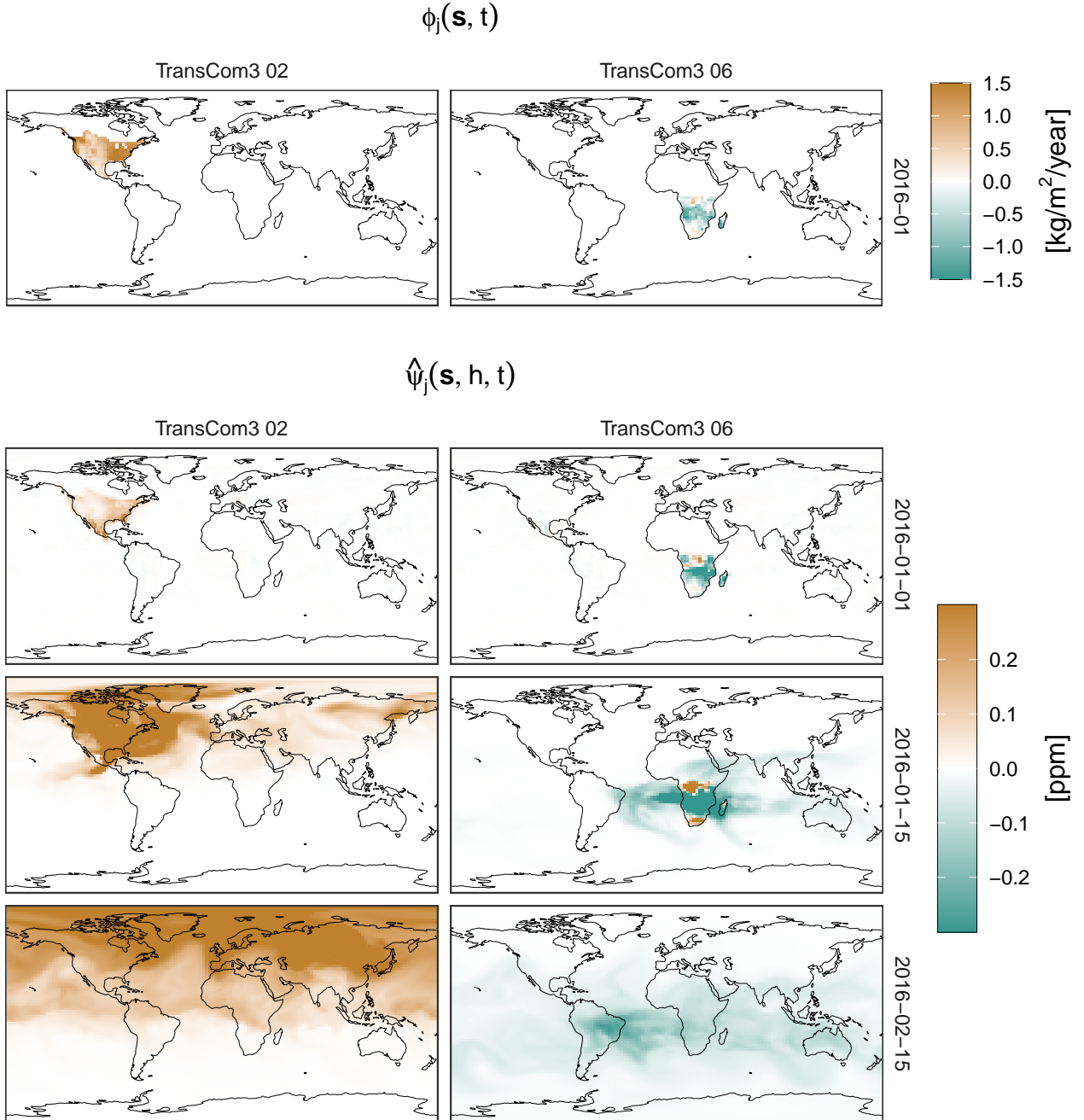


Fig. 2: Examples of flux basis functions that have support in the month of January 2016 in the regions TransCom3 02 and TransCom3 06, and the corresponding mole-fraction basis functions. The first row shows the values of the flux basis functions, $\phi_j(\cdot, \cdot)$, averaged over the whole month (these basis functions are zero outside January 2016). The next three rows show daily averages of the column-averaged CO₂ for the corresponding mole-fraction basis functions on three days: the start of the month-long period where the flux is non-zero, 01 January 2016; the middle of the period, 15 January 2016; and 15 days after the end of the period, 15 February 2016.

applied to the XCO₂ retrievals. The bias-corrected retrievals were then grouped and averaged into 1 s bins, and then they were further grouped and averaged into 10 s bins. The 10 s spans correspond to ground swathes of approximately 67 km in length. The standard deviation for each 10 s retrieval was computed as a function of the individual retrieval standard deviations, with an additional model–data mismatch term added to account for the expected differences arising from transport-model errors. For the MIP, the 10 s averages were assumed to be independent but, following Section 2.4, we treat them as dependent. As the prescribed variances already account for transport-model error, we adopt Case (ii) of Section 2.4 in our model. For more details on how the 10 s averages were computed, including how the standard errors were derived, see Crowell et al. (2019).

The OCO-2 retrieval algorithm produces estimates of XCO₂. In equation (7), we encapsulate the retrieval algorithm in the observation operator, \hat{A}_i . Appendix B gives more details on this observation operator in the case of OCO-2 retrievals.

4.4.2 TCCON

TCCON is a network of ground-based sites measuring solar radiances in the near-infrared spectral band (Wunch et al., 2011a). Similar to the way OCO-2 retrievals are obtained, these measurements are converted to retrievals of column-averaged CO₂ (and other gases) using a retrieval algorithm. TCCON retrievals have been adjusted to agree with World Meteorological Organization (WMO) trace-gas measurement scales, and validated using aircraft data (Wunch et al., 2010). As both TCCON and remote sensing instruments retrieve column-averaged mole fractions, the TCCON data are an important validation resource (Wunch et al., 2011b). The MIP used TCCON column-averaged CO₂ retrievals from the GGG2014 release as validation data, including all retrievals available as of July 6, 2017. In the MIP, outliers and retrievals corresponding to soundings with high solar zenith angle were removed. The remaining retrievals were then averaged over 30-minute intervals; further details are given by Crowell et al. (2019). We note that the filtering procedure used in the MIP occasionally led to long periods of time for which data were considered missing. For consistency with the MIP, in this study we used the same retrievals and postprocessing methods; the stations used are listed in Table 2.

Like OCO-2, TCCON retrievals also have an associated observation operator \hat{A}_i . This has a similar form to the operator for OCO-2, which is described in Appendix B. A detailed description of the TCCON observation operator is given by Wunch et al. (2011b).

4.5 Prior distributions over the parameters

The prior distributions for the parameters governing the scaling factors, α , are specified separately for the land and ocean TransCom3 regions. The land regions, which are observed directly by OCO-2 when in LG or LN mode, are assigned a non-informative prior, while the indirectly observed ocean regions (which also have relatively small fluxes over a given area) are assigned a relatively informative prior. Informative priors for ocean fluxes were deemed necessary following OSSEs performed by us, which revealed that it is often not possible to reliably constrain ocean fluxes from OCO-2 land data.

Specifically, for j corresponding to a land region, we assigned a prior to κ_j by letting $a_{\kappa,j} = b_{\kappa,j} = 1$ (resulting in a uniform prior), and for $\tau_{w,j}$ we let $\nu_{w,j} = 0.354$ and $\omega_{w,j} = (1 - \kappa_j^2)/0.0153$. This prior on $\tau_{w,j}$ implies that $1/\tau_{w,j}$, the marginal variance of the elements of the scalings in α that correspond to land regions, has 5% and 95% percentiles of 0.01 and 10, respectively, which is reasonably uninformative. For j corresponding to an ocean region, we apply an independent and identically distributed Gaussian prior with mean zero and standard deviation 0.5 to α_j . This is achieved by fixing $\kappa_j = 0$ and $\tau_{w,j} = 4$.

As described in Section 4.4.1, the OCO-2 MIP 10 s averages come with prescribed uncertainties that include both measurement error and transport-model error. This falls under Case (ii) of Section 2.4, so the parameters governing these processes are γ_g , ρ_g , and $\ell_{g,1}$. For the prior distribution of γ_g , we let $\nu_{\gamma_g} = 1.627$ and $\omega_{\gamma_g} = 2.171$, which lead to 5% and 95% prior percentiles of 0.5 and 10, respectively, while we used a uniform prior distribution for ρ_g . For $\ell_{g,1}$, we let $\nu_{\ell_{g,1}} = 1$ and $\omega_{\ell_{g,1}} = 1 \text{ min}^{-1}$. When doing bias correction online, we used the prior on β described in Section 2.4.

Table 2: Names of the TCCON stations used in this study.

Name	Reference
Ascension Island, Saint Helena	Feist et al. (2014)
Bialystok, Poland	Deutscher et al. (2015)
Bremen, Germany	Notholt et al. (2014)
Caltech, Pasadena, CA, USA	Wennberg et al. (2015)
Darwin, Australia	Griffith et al. (2014a)
Edwards (Armstrong/Dryden), CA, USA	Iraci et al. (2016)
Eureka, Canada	Strong et al. (2016)
Izaña, Spain	Blumenstock et al. (2014)
Karlsruhe, Germany	Hase et al. (2015)
Lamont, OK, USA	Wennberg et al. (2016)
Lauder, New Zealand	Sherlock et al. (2014)
Manaus, Brasil	Dubey et al. (2014)
Orléans, France	Warneke et al. (2014)
Park Falls, WI, USA	Wennberg et al. (2014)
Réunion Island, France	De Mazière et al. (2014)
Saga, Japan	Kawakami et al. (2014)
Sodankyla, Finland	Kivi et al. (2014)
Tsukuba, Japan	Morino et al. (2016)
Wollongong, Australia	Griffith et al. (2014b)

4.6 Computation

Computations were performed in two stages. In the first stage, the 682 mole-fraction basis functions were precomputed in the manner described in Section 4.2. This is the most computationally demanding step, as each basis function requires the CTM to be run for several days of clock time, on average. Fortunately, since every basis function can be computed independently from all others, computing them is an embarrassingly parallel problem. Furthermore, since the basis functions are shared between the different inversions in this section, they only need to be computed once. Computation of the basis functions took seven days in total using the Gadi supercomputer at the Australian National Computational Infrastructure.

The inversions were performed in the second stage. As mentioned in Section 2.5, the posterior distribution for each inversion was estimated using an MCMC sampling scheme, with details given in Appendix A. The sampling schemes in all cases were run for 11,000 iterations, and the first 1,000 iterations were discarded as burn-in. Convergence of the MCMC chain was assessed by inspection of all the trace plots. The scheme was implemented in the R programming language (R Core Team, 2020), with intensive linear algebraic computations offloaded for performance to a graphics processing unit (GPU) using Tensorflow (Abadi et al., 2016). The total running time of the sampler depended on which model assumptions were used; in particular, whether uncorrelated (15 minutes) or correlated errors (two hours) were modelled. All inversions were performed on a machine with an 8-core Intel i9-9900K CPU running at 3.60 GHz and an NVIDIA RTX 2080 GPU.

5 Results

In this section we evaluate WOMBAT, first in an OSSE, where the true fluxes are assumed known and data are simulated from these true fluxes, then on actual satellite data via the MIP protocol of Crowell et al. (2019). Using an OSSE, described in Section 5.1, serves two purposes: first, to show that WOMBAT can indeed recover the true fluxes in a controlled environment where the “working model” is the “true model”; and second, to illustrate the importance of modelling measurement-error biases and correlated errors when these are present in the true model from which the data are simulated. Then, in Section 5.2, we show that WOMBAT gives similar flux estimates to those obtained by different MIP participants, and that it performs

well relative to the MIP participants in reproducing out-of-sample TCCON validation data. In Section 5.3 we show that WOMBAT is able to estimate bias coefficients online, if needed.

5.1 Observing System Simulation Experiment (OSSE)

In this section we illustrate the use of WOMBAT in an OSSE, where we randomly draw flux scaling factors $\boldsymbol{\alpha}^s$ from a Gaussian distribution with mean $\mathbf{0}$ and covariance matrix $0.09\mathbf{I}$, and assume that these are the true flux scaling factors. We further assume that the dimension-reduction error, $\nu_1(\cdot, \cdot)$, is zero, so that the (simulated) true flux $Y_1^s(\cdot, \cdot)$ is given by

$$Y_1^s(\cdot, \cdot) = Y_1^0(\cdot, \cdot) + \sum_{j=1}^r \phi_j(\cdot, \cdot) \alpha_j^s, \quad (17)$$

where α_j^s is the j th element of $\boldsymbol{\alpha}^s$. The (simulated) true mole-fraction field, $Y_2^s(\cdot, \cdot, \cdot)$, is then given by

$$Y_2^s(\cdot, \cdot, \cdot) = Y_2^0(\cdot, \cdot, \cdot) + \sum_{j=1}^r \hat{\psi}_j(\cdot, \cdot, \cdot) \alpha_j^s. \quad (18)$$

Finally, we simulate measurements from the mole-fraction data model in equation (9) at the same times and locations as the OCO-2 10 s average retrievals for the LN and LG modes, by passing $Y_2^s(\cdot, \cdot, \cdot)$ through the corresponding OCO-2 observation operators (see Section 4.4.1).

When simulating data via (9), we assume that both \mathbf{b}_g and $\boldsymbol{\xi}_g$ are present. For the bias term \mathbf{b}_g , we assume that the OCO-2 retrieval biases are a linear combination of covariates that are associated with bias in the retrieval process:

- “dp”: The prior–retrieval surface pressure differential;
- “logDWS”: The logarithm of the total retrieved optical depth associated with the aerosol types dust, water cloud, and sea salt; and
- “co2_grad_del”: The difference between the retrieved CO₂ mole fractions at the surface and retrieval vertical level 13 (corresponding to the height with air pressure equal to 63.2% of the surface pressure, around 520–650 hPa for most retrievals).

The “official” V7r bias-correction parameters (regression coefficients) for the original Level 2 (L2) data release were obtained through offline comparison of the raw L2 product with TCCON retrievals, and they are the same for both LG and LN observations. They are equal to 0.3, 0.028, and 0.6, for the three variables, respectively. We construct our (simulated) true biases based on these coefficients.

To mimic the MIP setup, we assume that we are in Case (ii), wherein the prescribed variance of each retrieval needs to be inflated, and the inflated variance is the sum of the variance from both the correlated ($\boldsymbol{\xi}_g$) and uncorrelated ($\boldsymbol{\epsilon}_g$) error components. In our OSSE, we assume that the inflation factor of the prescribed variances, \mathbf{v}_g^{ps} , is $\gamma_g = 1.25$, and that the proportion of this variance allocated to the correlated error process is $\rho_g = 0.8$. We induce the correlations using the exponential covariance function described in Section 3 with the single length scale of the correlated component set to $\ell_{g,1} = 1$ minute for all $g = 1, \dots, n_g$. We specify this correlation structure to be the same for both LG and LN data.

We ran four different setups in WOMBAT, where bias is assumed or not assumed to be present, and where errors are assumed or not assumed to be correlated. The known true flux, generated as described above, is the same between the cases, and we evaluate the ability of WOMBAT to recover the truth under each of the setups. Table 3 gives the root-mean-squared error (RMSE) and continuous ranked probability score (CRPS, Gneiting and Raftery, 2007) when estimating monthly- and regionally-aggregated fluxes using these four setups. The regions on which these evaluations are based are the same TransCom3 regions that were used to construct the flux basis functions (see Section 4.2), and the quantities in the table are averages across all combinations of the 31 months and 22 regions. The true data-generating process involves both bias and correlated error. Therefore, as one would expect, Table 3 shows that the WOMBAT setup that takes into account both of these features performs the best in terms of both RMSE and CRPS, while

Table 3: Root-mean-squared error (RMSE) and continuous ranked probability score (CRPS) when estimating monthly regional fluxes using LG and LN data in the OSSE of Section 5.1. Four setups in WOMBAT are evaluated and the regions and time periods over which these summaries (averages) are obtained are the same as those used for constructing flux basis functions (see Section 4.2).

Configuration	RMSE		CRPS	
	LG	LN	LG	LN
Bias correction/correlated errors	0.023	0.021	0.010	0.009
Bias correction/uncorrelated errors	0.038	0.038	0.015	0.016
No bias correction/correlated errors	0.045	0.026	0.016	0.011
No bias correction/uncorrelated errors	0.092	0.063	0.034	0.026

the setup that assumes that neither feature is present performs the worst. For the two partially misspecified setups, the bias-corrected/uncorrelated setup outperforms the not-bias-corrected/correlated setup for LG data, while the opposite is true for LN data. Notably, despite the presence of systematic biases in the simulated data, the WOMBAT setup that assumes no bias, but which takes into account correlated errors, performs overwhelmingly better than the fully misspecified model that assumes no bias and uncorrelated errors.

Figure 3 shows the (simulated) true (black), prior mean (blue), and posterior distributions (red, purple, orange, and green), for the total flux in the tropics (latitude 23.5°S–23.5°N) in 2015 and 2016, from both LN and LG, split by the southern and the northern components (latitudes 23.5°S–0° and 0°–23.5°N, respectively). The four posterior distributions depicted in each panel correspond to the four different WOMBAT setups. The interior of the ellipses represent the 95% credible regions. The grey dotted lines along the diagonal correspond to combinations of the southern and northern fluxes that yield the true total flux in the tropics; if the dotted line is not within the ellipse for an inversion, the total flux is misestimated. All shown fluxes are exclusive of fossil fuels which, recall, are held fixed in the inversions. Figure C2 in Appendix C shows the results on a global scale (land vs ocean), while Figure C3 in Appendix C shows the results on a regional scale (TransCom3 region 04 [South American Temperate] vs TransCom region 06 [Southern Africa]).

Collectively, the performances of the different models, as shown in Figures 3, C2, and C3, align with the conclusions based on the CRPS and RMSE statistics. In all the cases shown, the 95% credible regions for the WOMBAT configuration with both bias correction and correlated error (red) contain the true value, while those for the configuration with neither feature (green) do so rarely. The credible regions for the bias-corrected/uncorrelated variant (orange) are always smaller than the red credible regions, indicating that the bias-corrected/uncorrelated variant is overconfident. In contrast, the purple credible regions, for the not-bias-corrected/correlated variant, are always larger, which may suggest that the correlated errors are partially compensating for the lack of bias correction in this variant.

In summary, this OSSE shows that WOMBAT can recover the true flux when the assumed model is the true model. But, more importantly, the OSSE also demonstrates the importance of modelling both bias and correlated errors in inversions. If the bias parameters are omitted, fluxes can be estimated incorrectly, although this may be partially mitigated by modelling correlated errors. If uncorrelated errors are assumed, estimation performance suffers, and flux estimates will likely be reported with too small an uncertainty, even if the prescribed variances are allowed to be inflated when making inference. Practically, in a real-data setting, any factors thought to introduce systematic biases should be taken into account, but this OSSE also suggests that the use of correlated errors may provide some insurance against any remaining, unmitigated, spatio-temporal biases.

5.2 OCO-2 satellite data

In this section we present results from WOMBAT applied to OCO-2 satellite data under the MIP protocol (Crowell et al., 2019). The protocol mandates the use of OCO-2 retrievals with the TCCON-based offline bias correction. While WOMBAT is capable of online bias correction (see Section 5.3), in this section we

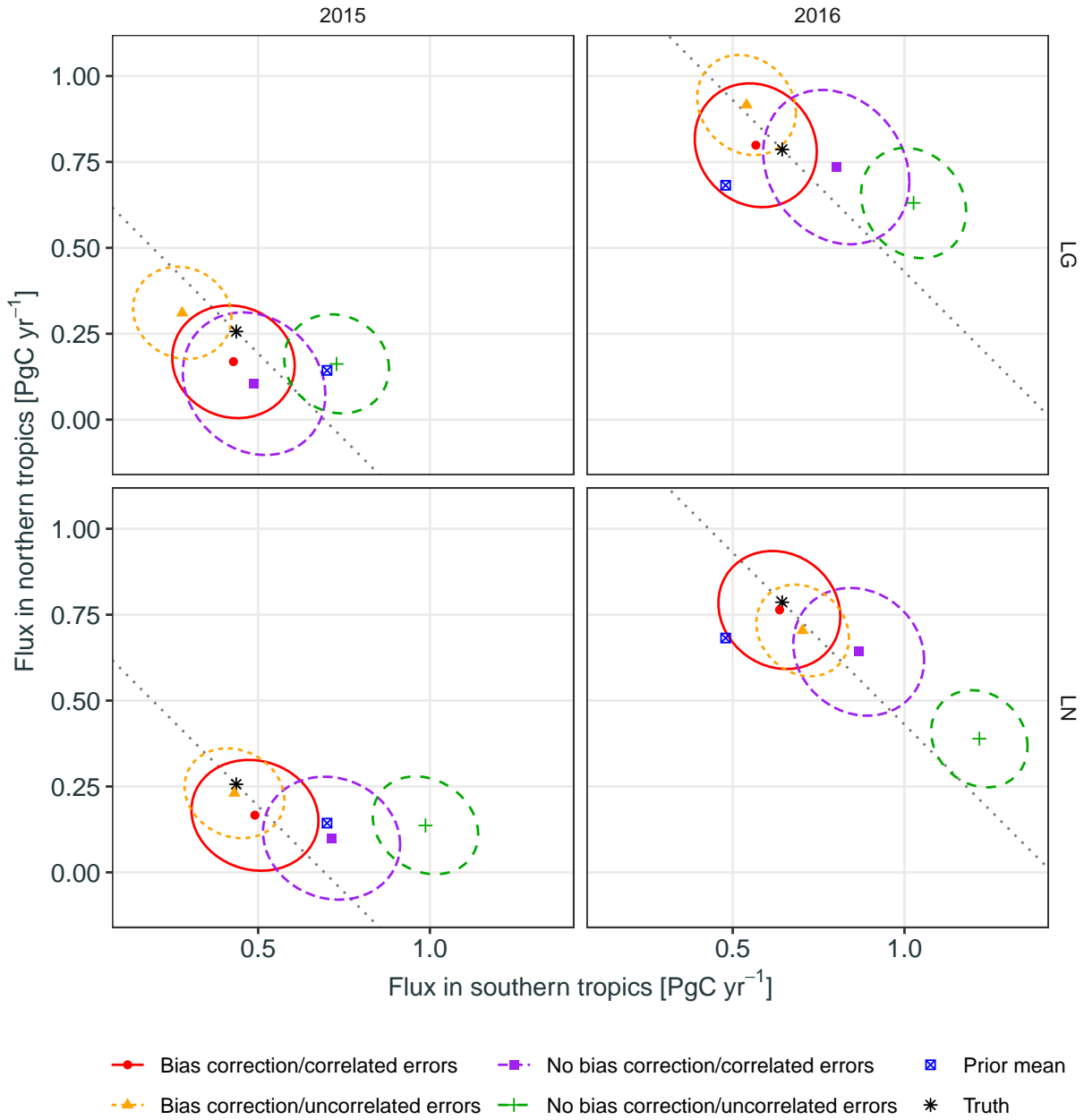


Fig. 3: True, prior, and posterior, estimates of total flux in the northern tropics (0° – 23.5° N) versus the total flux in the southern tropics (23.5° S– 0°) for the OSSE in Section 5.1. The columns correspond to the years 2015 and 2016, while the rows show which observation groups were used, either OCO-2 land glint (LG) or land nadir (LN), noting that the prior and true flux are the same across rows. Points show the posterior mean fluxes for each model configuration, as well as the prior mean in blue and the truth in black. For the posterior quantities, the ellipses contain 95% of the posterior probability. The grey dotted lines along the diagonal correspond to combinations of southern and northern tropical flux that yield the true total flux in the tropics. All fluxes are exclusive of fossil fuels, which are held fixed in the inversion.

follow the protocol and set the bias parameters in WOMBAT equal to zero. Moreover, since we are currently unable to deconvolve dimension-reduction error from other sources of error (e.g., transport-model error) in our model, we do not include $v_1(\cdot, \cdot)$ in (1), and let its impact on the mole-fraction field, $v_{2,1}(\cdot, \cdot, \cdot)$ in (5), be absorbed into the correlated error term, ξ_g .

5.2.1 Flux comparison on a region-time basis with the MIP

In the OCO-2 MIP, nine participants submitted fluxes based on inversions satisfying the MIP protocol. Each participant reported to the MIP four sets of fluxes: their prior mean fluxes, and fluxes from three inversions based respectively on point referenced data, OCO-2 LG data, and OCO-2 LN data. Crowell et al. (2019) considered the different participants’ fluxes as an ensemble, reporting the ensemble mean, median, and standard deviation across a variety of temporal and spatial scales. Under the same protocol and using OCO-2 LG and LN data, we compare WOMBAT’s posterior distribution over the fluxes to the corresponding results from the MIP ensemble.

Through its MCMC scheme, WOMBAT’s inversions generate samples from the posterior distribution of $Y_1(\cdot, \cdot)$, the flux field. These samples enable estimation of functionals of the posterior distribution, including posterior means and quantiles. While some individual MIP participants are able to produce probabilistic uncertainty estimates for fluxes, these were not reported as part of the MIP; instead, the empirical distribution from the ensemble of fluxes was used by the MIP for uncertainty quantification. Since it is difficult to make a quantitative comparison between WOMBAT’s posterior-based uncertainties and the ensemble uncertainties in the MIP, we opt here for a qualitative analysis, where the posterior distributions over the fluxes are visually compared to the ensemble minimum, mean, and maximum. This comparison is done at both annual and monthly temporal scales, and across spatial scales encompassing the whole globe, global land, global ocean, and zonal bands.

Global totals: Figure 4 presents annual and monthly non-fossil-fuel fluxes for the globe, land regions, and ocean regions. Fluxes are shown for the MIP, split into prior, LG inversions, and LN inversions, and for WOMBAT, split into prior, posterior using LG data, and posterior using LN data. Thick lines show the ensemble means for the MIP, and the (prior or posterior) means for WOMBAT. Shaded areas and thin lines for the MIP denote the values between the ensemble minimum and maximum, while for WOMBAT they denote values in the 95% credible intervals.

At the global scale, shown in the first row of Figure 4, the MIP ensemble mean for prior fluxes over land and WOMBAT’s prior mean over land are similar. This likely reflects the common use of prior inventories between groups performing flux inversions, particularly biospheric fluxes based on the CASA biogeochemical model (see Section 4.1 and Table 1). By contrast, WOMBAT’s prior ocean fluxes are deeper than any other member of the MIP ensemble. The global annual non-fossil-fuel fluxes estimated by posterior means from WOMBAT are very similar for both LG and LN modes, with an overall posterior mean net sink in 2015 of 3.40 and 3.14 PgC yr⁻¹, respectively, and in 2016 of 4.14 and 4.27 PgC yr⁻¹, respectively. For 2015, these sinks are very similar to the MIP ensemble means (3.57/3.21 PgC yr⁻¹ for LG/LN, respectively) for both modes while, for 2016, WOMBAT returns a deeper posterior-mean sink than the MIP ensemble means (3.82/3.78 PgC yr⁻¹ for LG/LN, respectively), although the 95% credible intervals overlap with the ensemble spread. At a monthly scale, WOMBAT reproduces a key feature of the MIP fluxes, wherein the seasonal cycle in the fluxes, driven by the Northern Hemisphere growing season, begins and ends earlier than in the prior for both 2015 and 2016. In agreement with the MIP, WOMBAT results indicate that the peak sink in the cycle is larger than that in the prior. However, the sink estimated by WOMBAT is around 0.4 PgC mo⁻¹ smaller than the MIP ensemble mean for both LG and LN.

Global land and ocean: For global land fluxes, shown in the second row of Figure 4, WOMBAT’s results agree with those from the MIP for both LG and LN in that a source larger than the prior flux is estimated for October 2015. However, while the source persists into November in the MIP ensemble mean, it does not do so in the WOMBAT posterior mean. For global ocean fluxes, shown in the third row of Figure 4, the MIP LG- and LN-estimated fluxes differ little from the prior fluxes, and we observe the same for global oceans in the WOMBAT estimates for both LG and LN modes and in most months. The exceptions are September and October in both years, where WOMBAT estimates a shallower sink, and even zero flux with

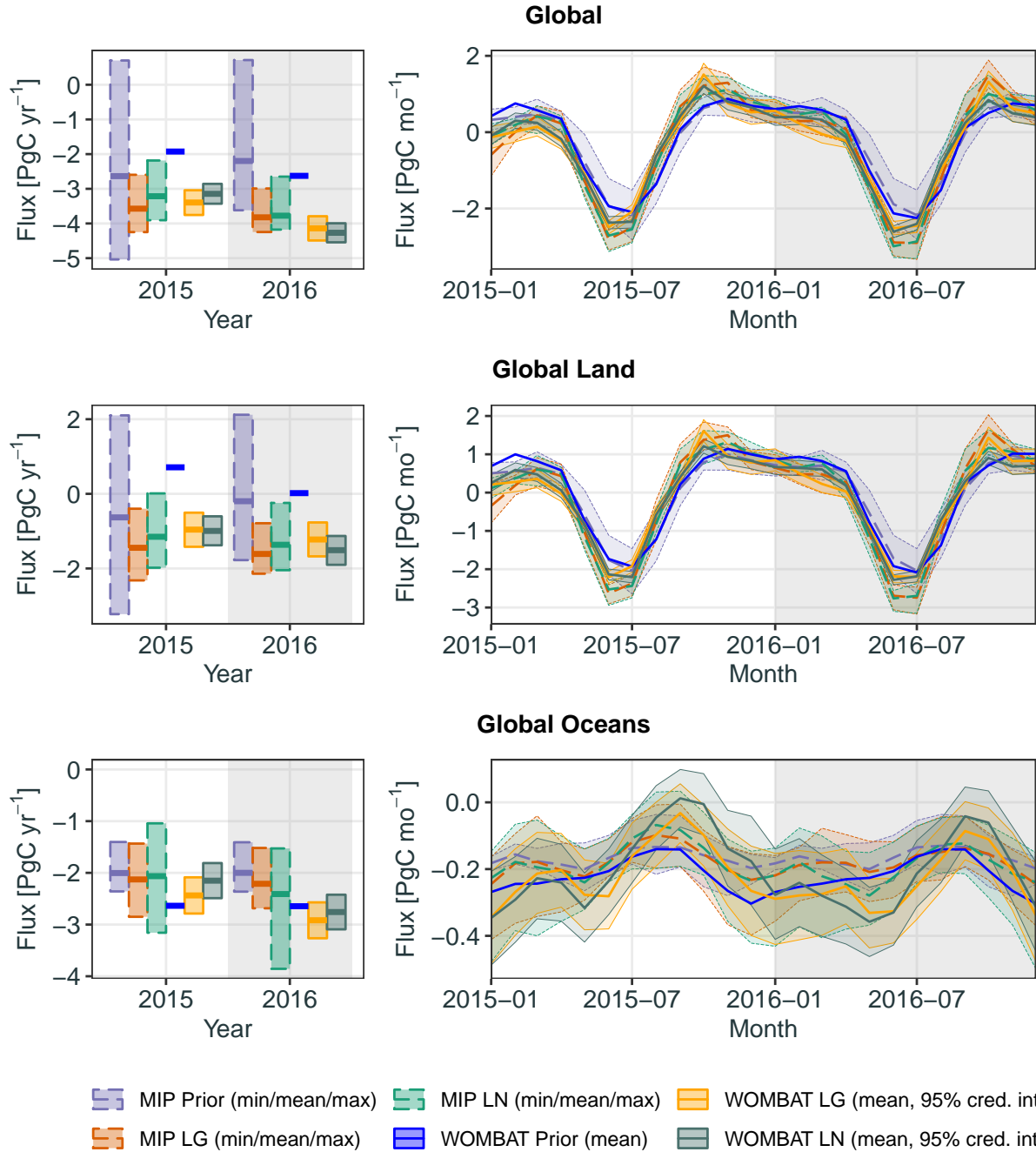


Fig. 4: Annual (left column) and monthly (right column) fluxes for the globe (first row), land (second row), and ocean (third row). Flux estimates from both the MIP and WOMBAT are shown, split into the prior, LG inversions, and LN inversions. Thick lines represent the ensemble means for the MIP and the (prior or posterior) means for WOMBAT. Shaded areas and thin lines for the MIP represent values between the ensemble minimum and maximum, while for WOMBAT they represent values in the 95% credible intervals. Fossil-fuel fluxes are excluded from all figures. Note that each row of plots has a different vertical scale.

the LN data. These features are not obvious in the MIP ensemble means, but appear reasonable within the ensemble spread.

Zonal bands: Figure C4 in Appendix C shows fluxes for zonal bands covering the northern extratropics (23.5°N–90°N), northern tropics (0°–23.5°N), southern tropics (23.5°S–0°), and southern extratropics (90°S–23.5°S). For the MIP ensemble, Crowell et al. (2019) noted that inversions using LG data led to a smaller net annual sink (averaged between 2015 and 2016) in the northern extratropics than those using LN data. WOMBAT also finds this feature, with a 95% credible interval of the difference spanning 0.14–0.6 PgC yr⁻¹. This is substantially smaller than the difference between the MIP ensemble means for these modes, which is 0.7 PgC yr⁻¹. Fluxes in the southern extratropics, shown in the fourth row of Figure C4, are dominated by ocean fluxes for which, as noted above, LG and LN data provide little information.

One of the most prominent features in the MIP inversion results is a seasonal cycle in the tropics that is larger than that in both the prior mean and the *in situ* inversions (Crowell et al., 2019). From the second and third rows of Figure C4, which depict tropical-zone fluxes, it can be seen that WOMBAT does not reproduce this for both LG and LN inversions. In the northern tropics, the WOMBAT posterior means are similar to the prior means, and the credible intervals in the annual fluxes reflect high confidence. However, WOMBAT results do corroborate those of the MIP ensemble, in that non-fossil-fuel fluxes in the northern tropics were a net source of CO₂ in 2016.

5.2.2 TCCON comparison

To evaluate the estimated fluxes in the OCO-2 MIP, each participant was asked to compare the 30-minute-average TCCON retrievals of column-averaged CO₂ (see Section 4.4.2) to the column-averaged CO₂ predicted under the corresponding estimated fluxes and CTM used for the inversion. Recall that, when performing the inversions, only OCO-2 data were used, and the TCCON data were treated as unobserved and used for validation. For WOMBAT, we repeated this validation exercise by examining the prior and posterior distributions of $\mathbf{Z}_{2,g}$, where each g corresponds to a different TCCON site. For each group g , we set $\mathbf{b}_g = \mathbf{0}$, since we assume that the provided TCCON retrievals are free of bias. On the other hand, we assumed that $\boldsymbol{\xi}_g + \boldsymbol{\epsilon}_g$ has variance that is group specific, and that these errors are fully correlated. While this assumption is conservative, it is also reasonable, since it is likely that the CTM does induce errors that are highly correlated in time at a common spatial location, as it averages all variables on a rather coarse grid when simulating atmospheric transport. We estimate the variance of these correlated errors in a group g as the average of the reported variances of each TCCON retrieval within a group g .

In Figure C5 in Appendix C we compare the time series of the TCCON retrievals with the predictions from WOMBAT under the prior mean flux, the posterior distribution of flux from LG data, and the posterior distribution of flux from LN data. Several things are of note from this figure: First, the posterior-mean estimates are a better match to the TCCON retrievals than the prior-mean estimates, which is evidence that OCO-2 data allow for improved flux estimates. Second, discrepancies between TCCON and predicted retrievals persist for a long time, lending credence to our assumption that errors are highly temporally correlated. Third, the 95% prediction intervals are appropriate, and largely contain within them the TCCON retrievals.

In Figure 5 we reproduce an augmented version of Figure 8 of Crowell et al. (2019), which depicts the mean and standard deviation of the differences between the TCCON retrievals and the predicted retrieval by TCCON site, MIP participant, and observation mode (LG and LN) alongside the results from WOMBAT. The improvement of the WOMBAT posterior prediction over the prior prediction is evident in the mean of the differences, and the WOMBAT posterior error means and standard deviations are in line with those of the MIP participants. WOMBAT’s predictive distributions from LG-inferred fluxes can be seen to be better than those of the MIP participants, even by straightforward visual inspection. In Table 4 we compute mean-squared error by participant and observation mode averaged over all the TCCON stations. WOMBAT outperforms all other participants when using this metric with LG data, and is fourth-best when using this metric with LN data. While these results are not conclusive on the validity of the WOMBAT fluxes globally, they are encouraging, especially in light of the fact that our flux process has a relatively low-dimensional representation.

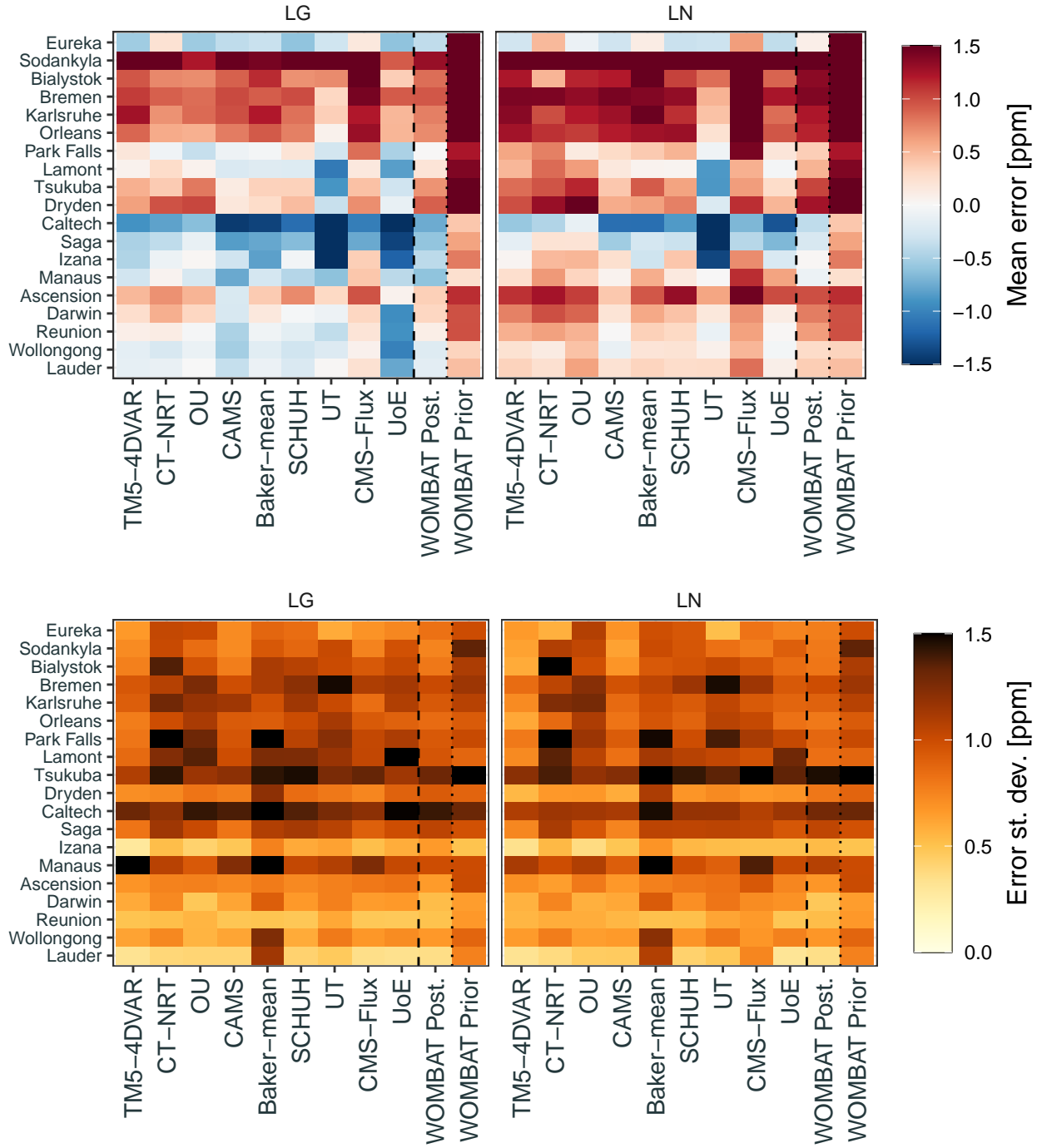


Fig. 5: Mean (top row) and standard deviation (bottom row) of the errors across TCCON stations for each MIP participant (refer to Crowell et al., 2019, for details) and for WOMBAT’s prior and posterior mean predicted values. The error statistics for inversions using LG data are shown in the left column, while those for LN data are shown in the right column. This figure reproduces and extends Figure 8 of Crowell et al. (2019) with similar (but not identical) colour gradients.

Table 4: Mean-squared error (in ppm²) averaged across TCCON stations, for each MIP participant and for WOMBAT’s prior and posterior mean predicted values.

	TM5-4DVAR	CT-NRT	OU	CAMS	Baker-mean	SCHUH	UT	CMS-Flux	UoE	WOMBAT Post.	WOMBAT Prior
LG	1.33	1.63	1.31	1.31	1.88	1.41	1.85	1.78	1.71	1.19	3.56
LN	1.36	2.09	1.74	1.24	2.12	1.58	1.71	2.72	1.37	1.57	3.56

Table 5: Posterior means, 2.5% quantiles, and 97.5% quantiles, for the parameters $\ell_{g,1}$, γ_g , and ρ_g , for the inversions using LG and LN retrievals. Recall that the parameters associated with LG and LN are derived from different inversions, and not from using the two retrieval groups in the same inversion.

Variable	LG			LN		
	Mean	2.5%	97.5%	Mean	2.5%	97.5%
$\ell_{g,1}$	1.221	1.183	1.261	1.106	1.072	1.137
γ_g	1.207	1.187	1.226	1.209	1.190	1.226
ρ_g	0.834	0.829	0.838	0.835	0.831	0.840

5.2.3 The inferred parameters

One of the key features of WOMBAT is the use of a hierarchical prior distribution, which applies to both the parameters governing the flux scaling factors, and to the parameters governing the model–data discrepancy and measurement-error processes. Figure 6 shows the estimated posterior means and 95% credible intervals for the autoregressive parameters κ (top) and the innovation precisions τ_w (bottom), for the 11 land regions, and for inversions using LG and LN data. The inferred parameters are relatively consistent across the LG and LN modes, with the exception of TransCom3 region 02 (North American Temperate). Most regions have a posterior mean for κ_j that is approximately between 0.25 and 0.75, reflective of moderate autocorrelation in the scaling factors. The exception is TransCom3 region 03, for which the scaling factors are estimated to be highly autocorrelated *a priori*. The innovation precisions, τ_w , have posterior means that lie approximately between 1 and 10, for most regions.

The parameters governing the model–data discrepancy and measurement-error processes are ρ_g , $\ell_{g,1}$, and γ_g , for $g = 1, \dots, n_g$. Table 5 gives the posterior means, 2.5% quantiles, and 97.5% quantiles, for these parameters. Recall that the LG and LN parameters are derived from different inversions; they are not two groups in the same inversion. Nonetheless, the inferred parameters are similar between the inversions, which is reassuring. The values for γ_g are indicative of a 21% variance inflation needed for both instrument modes. The length scales, ℓ_g , are 1.2 minutes for the LG data and 1.1 minutes for the LN data, which corresponds to around 700–800 km on the ground. Finally, the estimated values of ρ_g are around 0.835, indicating that the majority of the combined model–data discrepancy/measurement-error process should indeed be attributed to the correlated component, ξ_g , given in (9).

5.3 Online bias correction

The OSSE-based sensitivity study in Section 5.1 demonstrated that WOMBAT is able to perform *online* bias correction with simulated data, where biases are estimated while doing flux inversion. This is different to the typical *offline* approach to bias correction, where retrieval biases are determined in a separate study. To comply with the MIP protocol, the online bias-correction functionality of WOMBAT was disabled in the study of Section 5.2, and the TCCON-based offline bias-corrected OCO-2 10 s average retrievals from the MIP were used. In order to investigate the prospect of online bias correction with real data, we repeat the

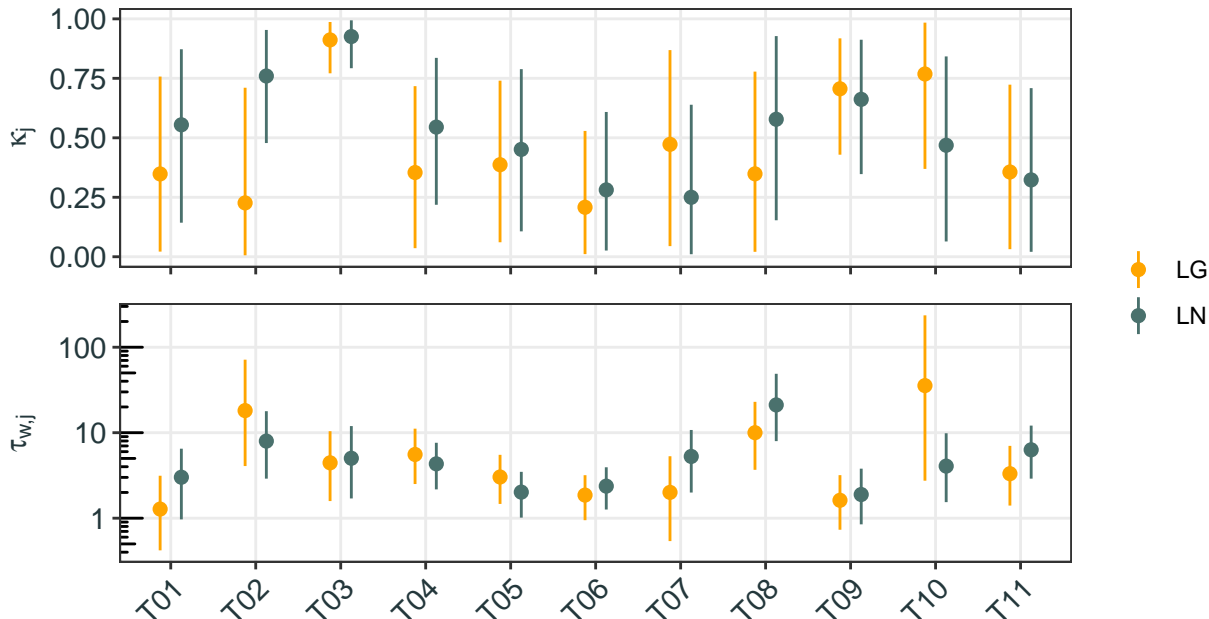


Fig. 6: Posterior means and 95% credible intervals for κ (top) and τ_w (bottom, shown using a log scale), for the 11 land regions: TransCom3 region 01 (T01) to TransCom3 region 11 (T11). Estimates are shown for inversions using LG data (yellow) and LN data (dark green).

inversions with online bias correction enabled, using OCO-2 10 s average retrievals both with and without the TCCON-based offline corrections.

In Figure 7 we show the posterior densities of the WOMBAT-estimated bias-correction coefficients when using the retrievals without the offline correction. The posterior densities shown there are for inversions based on LG and LN retrievals, while the TCCON-based offline bias-correction coefficients are given by the blue vertical lines. The WOMBAT-estimated coefficients have the same sign and similar magnitudes to the offline corrections, suggesting that WOMBAT is picking up similar bias patterns while doing flux inversion. However, with the exception of the “dp” coefficient under the LN inversion, the offline values are outside the plausible ranges estimated by WOMBAT. For “co2_grad_del”, WOMBAT favours a smaller correction for both LG and LN, while for “logDWS” a larger correction is favoured. For “dp”, WOMBAT favours a smaller correction under the LG inversion.

We repeated the online bias-correction procedure using retrievals retaining the TCCON-based offline bias correction. In this setting, if the retrievals are unbiased, bias coefficients equal to zero should be inferred. The posterior densities of the estimated coefficients under this configuration are shown in the second row of Figure 7. As expected, the magnitudes of the online-estimated coefficients are close to zero, although the credible intervals do not always include zero. Naïvely, one might expect that the coefficients would be approximately equal to the difference between the TCCON-based offline coefficients and the coefficients estimated by WOMBAT when using uncorrected data. For “dp” and “co2_grad_del”, the estimated coefficients indeed have the expected sign, and magnitudes of the expected order. The inferred “logDWS” coefficients are surprising, however, with an opposite sign to what was expected for the LG inversion, and with smaller magnitudes for both the LG and LN inversions. This unexpected result is a reflection of the complex interplay, and nonlinear relationships, between the parameters and processes in our model.

Overall, the online-estimated bias correction is practically, if not statistically, similar to the TCCON-based offline correction. One possible explanation for the difference between the WOMBAT and the TCCON-based estimates is that different data are used, because WOMBAT does not use TCCON data for the correction. Moreover, it is likely that the true bias coefficients are spatio-temporally varying; if this is indeed the case,

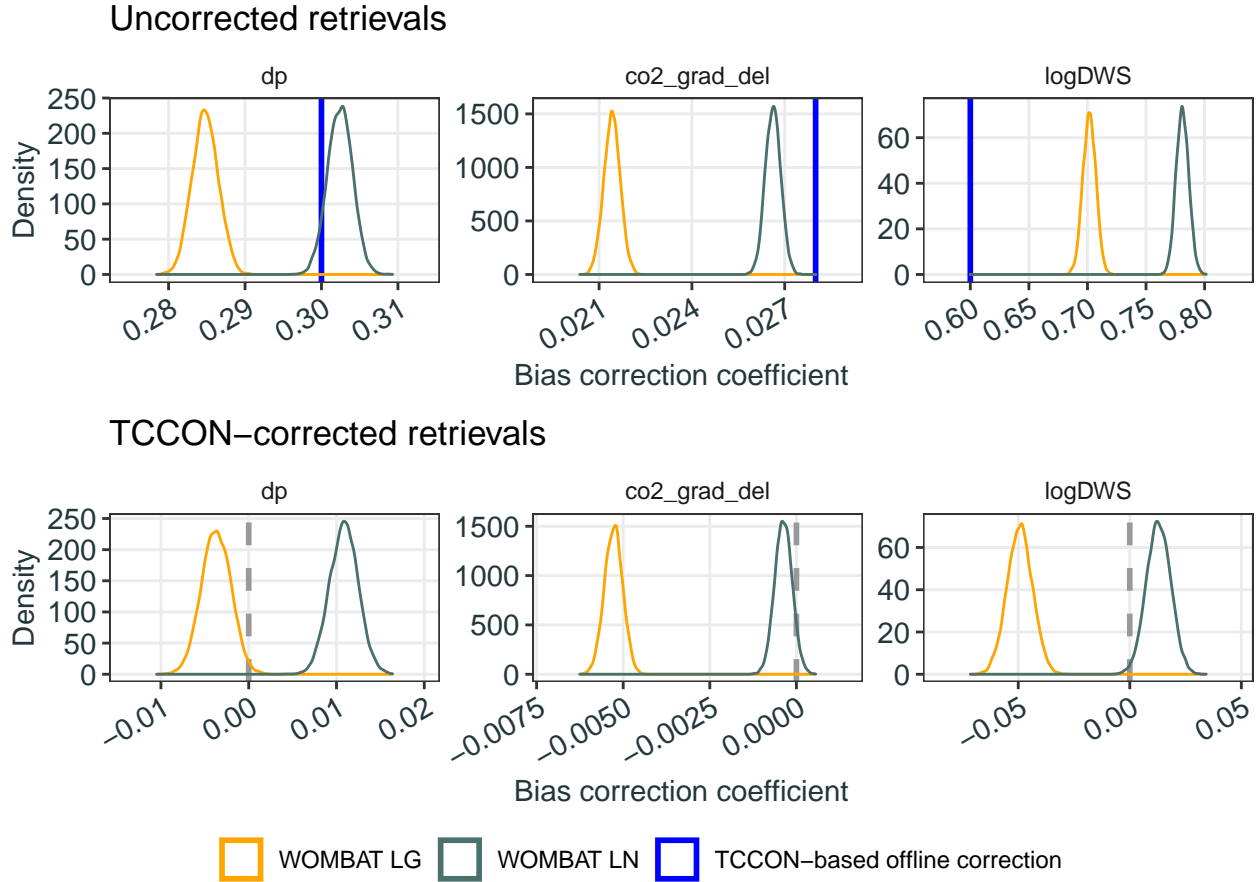


Fig. 7: Posterior densities of bias-correction coefficients from inversions using OCO-2 retrievals without bias corrections applied (top row), and those from inversions using retrievals corrected using the TCCON-based bias coefficients (bottom row). Densities are shown for inversions based on LG and LN retrievals in yellow and dark green, respectively. The TCCON-based offline bias correction coefficients are shown as vertical blue lines for the panels in the top row. The grey dashed lines in the bottom row mark zero, the value the coefficients would take if the data were unbiased.

the estimated biases would be affected by the spatio-temporal locations of the retrievals used to estimate them. Another reason may be that, for simplicity, we have used only a few of the most important variables that are used for offline bias correction; a consideration of all the variables may lead to slightly different results. Despite this, our results show that online bias correction is possible, and that further research into it as an attractive by-product of flux inversion is warranted.

Figure 8 gives annual and monthly fluxes estimated from the inversions using the online bias correction applied to the uncorrected retrievals. For comparison, the equivalent fluxes from Section 5.2.1, for the offline-corrected data and with the online bias correction disabled, are also reported. The annual and monthly fluxes are similar between the offline-corrected and online-corrected inversions, with substantial overlap in the marginal posterior distributions for all time periods. This result gives further evidence that online bias correction is a viable alternative to offline correction (here based on TCCON data) when doing flux inversion.

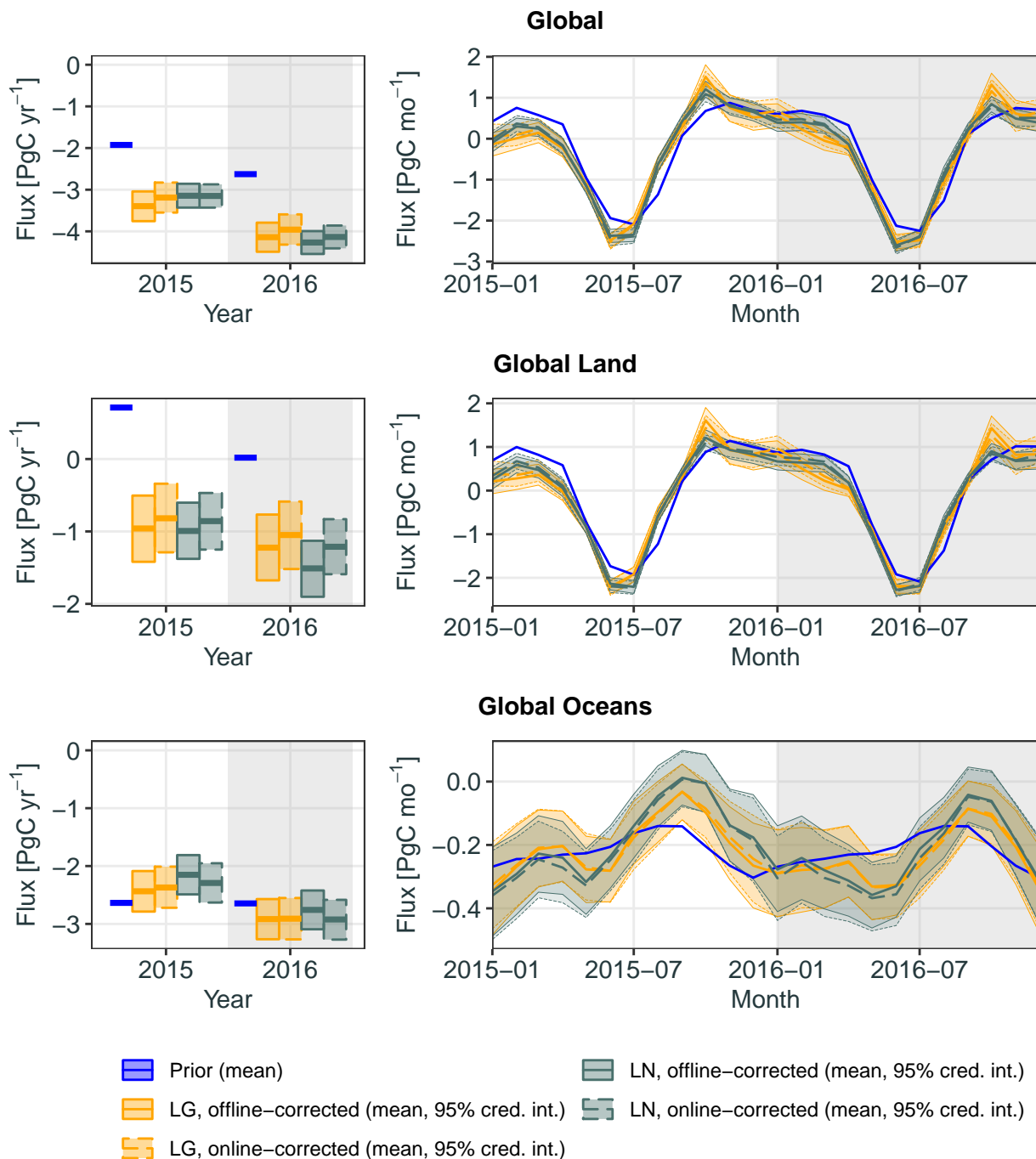


Fig. 8: Annual and monthly fluxes for WOMBAT inversions using: TCCON-based offline bias-corrected retrievals (solid lines with yellow for LG and dark green for LN; the fluxes are the same as in Figure 4), and with online bias correction applied to the uncorrected retrievals (dashed lines). The prior-mean fluxes are shown in blue. Solid lines depict prior/posterior means, and shaded areas denote the 95% credible intervals. The top row depicts global fluxes, the middle row global land fluxes, and the bottom row global ocean fluxes.

6 Conclusion

The Wollongong Methodology for Bayesian Assimilation of Trace-gases (WOMBAT) extends the standard Bayesian synthesis flux-inversion framework and is based on a fully Bayesian hierarchical statistical model. It incorporates physically motivated flux basis functions, and follows the standard Bayesian synthesis framework by using a CTM to compute the corresponding mole-fraction basis functions offline. The scaling factors for the basis functions are inferred from mole-fraction satellite data. WOMBAT incorporates a correlated error term, estimates measurement biases and measurement-error scaling factors online, estimates prior variances and length scales on flux scaling factors, and uses a fully Bayesian MCMC scheme that allows uncertainty quantification on all unknown parameters in the model. We have illustrated the importance of modelling correlation and bias within a flux-inversion system, and we have shown that WOMBAT produces global and regional flux estimates from OCO-2 data that are comparable to those from the MIP participants in Crowell et al. (2019). In particular, WOMBAT outperformed the other flux models in reproducing TCCON data when using the OCO-2 LG retrievals to obtain the fluxes, and it was competitive when using fluxes obtained from the OCO-2 LN retrievals. The MIP reported a global total (non-fossil-fuel) carbon sink of 3.7 ± 0.5 PgC yr⁻¹ (ensemble mean \pm ensemble standard deviation) and 1.5 ± 0.6 PgC yr⁻¹ for global land for the years 2015 and 2016. WOMBAT’s posterior estimates are 3.77 ± 0.09 PgC yr⁻¹ (posterior mean \pm posterior standard deviation) and 1.09 ± 0.14 PgC yr⁻¹, respectively, using the OCO-2 LG data, and 3.71 ± 0.07 PgC yr⁻¹ and 1.25 ± 0.13 PgC yr⁻¹, respectively, using the OCO-2 LN data. When the fossil-fuel fluxes are included, we estimate a global carbon source of 6.11 ± 0.09 PgC yr⁻¹ using the LG data, and 6.17 ± 0.07 PgC yr⁻¹ using the LN data. These estimates corroborate those of the MIP within uncertainty. The WOMBAT framework, and code to reproduce the results of this paper, are available online at <https://github.com/mbertolacci/wombat-paper/>.

This paper presents the general, underlying, Bayesian hierarchical framework for WOMBAT, which will serve as a baseline for our flux inversions based on current and future versions of OCO-2 data. There are several potential extensions being considered; here we discuss three of the most pertinent ones. First, WOMBAT, like most other flux-inversion systems, currently operates using a single CTM. This is problematic from a statistical modelling point of view, as it does not allow one to attribute the correlated error to the measurement-error process or the mole-fraction process. If more than one CTM is used, one could, in principle, statistically identify at least part of the error due to transport. This will not necessarily solve the problem though, since CTMs tend to share common features that induce similar correlations (e.g., due to unresolved sub-grid variation). A possible way forward is to take results from offline OSSEs to estimate and fix the parameters characterising the CTM error, and then attribute any residual observed correlation to the retrieval process. Second, WOMBAT extends a traditional state-space approach to flux inversion, which competes with adjoint models that can allow for a much higher flux dimensionality. Moving forward, WOMBAT will seek to introduce higher dimensionality by using approximations to response functions constructed from flux basis function that are at a much finer scale than the TransCom3-by-month spatio-temporal basis functions that we have used here. These will help reduce any model error due to dimensionality reduction. Finally, WOMBAT currently only models along-track correlations when modelling the correlation-error term ξ_g . However, the general framework we have proposed, based on the Vecchia approximation, can be extended to model full space-time correlations. Dedicated investigations will be required to assess the feasibility of the implementation, and the impact it will have on flux estimates.

Acknowledgements

This project was largely supported by the Australian Research Council (ARC) Discovery Project (DP) DP190100180. Andrew Zammit-Mangion’s research was also supported by an ARC Discovery Early Career Research Award (DECRA) DE180100203. Noel Cressie’s research was also supported by ARC DP150104576. Cressie’s and Zammit-Mangion’s research was also supported by NASA ROSES grant 17-OCO2-17-0012. Jenny Fisher was supported by ARC DP160101598. Ann Stavert and Matthew Rigby were supported by the UK Natural Environment Research Council grant NE/K002236/1. The TCCON data were obtained from the TCCON Data Archive hosted by CaltechDATA at <https://tccodata.org>. The authors would also like to thank David Baker for generating the OCO-2 10 s average retrievals, and several colleagues for valuable input/feedback. These include Beata Bukosa, Nicholas Deutscher, Anita Ganesan, Peter Rayner,

Andrew Schuh, and members of the OCO-2 Flux Team. This work was supported by resources provided by the Pawsey Supercomputing Centre with funding from the Australian Government and the Government of Western Australia. The work was also supported by the NCI National Facility systems at the Australian National University through the National Computational Merit Allocation Scheme supported by the Australian Government.

References

- Abadi, M., Agarwal, A., Barham, P., Brevdo, E., Chen, Z., Citro, C., Corrado, G. S., Davis, A., Dean, J., Devin, M., Ghemawat, S., Goodfellow, I., Harp, A., Irving, G., Isard, M., Jia, Y., Jozefowicz, R., Kaiser, L., Kudlur, M., Levenberg, J., Mane, D., Monga, R., Moore, S., Murray, D., Olah, C., Schuster, M., Shlens, J., Steiner, B., Sutskever, I., Talwar, K., Tucker, P., Vanhoucke, V., Vasudevan, V., Viegas, F., Vinyals, O., Warden, P., Wattenberg, M., Wicke, M., Yu, Y., and Zheng, X. (2016). TensorFlow: Large-scale machine learning on heterogeneous distributed systems. arXiv:1603.04467.
- Baker, D. F., Doney, S. C., and Schimel, D. S. (2006). Variational data assimilation for atmospheric CO₂. *Tellus B: Chemical and Physical Meteorology*, 58:359–365.
- Basu, S., Baker, D. F., Chevallier, F., Patra, P. K., Liu, J., and Miller, J. B. (2018). The impact of transport model differences on CO₂ surface flux estimates from OCO-2 retrievals of column average CO₂. *Atmospheric Chemistry and Physics*, 18:7189–7215.
- Basu, S., Guerlet, S., Butz, A., Houweling, S., Hasekamp, O., Aben, I., Krummel, P., Steele, P., Langenfelds, R., Torn, M., Biraud, S., Stephens, B., Andrews, A., and Worthy, D. (2013). Global CO₂ fluxes estimated from GOSAT retrievals of total column CO₂. *Atmospheric Chemistry and Physics*, 13:8695–8717.
- Bey, I., Jacob, D. J., Yantosca, R. M., Logan, J. A., Field, B. D., Fiore, A. M., Li, Q., Liu, H. Y., Mickley, L. J., and Schultz, M. G. (2001). Global modeling of tropospheric chemistry with assimilated meteorology: Model description and evaluation. *Journal of Geophysical Research: Atmospheres*, 106:23073–23095.
- Blumenstock, T., Hase, F., Schneider, M., García, O. E., and Sepúlveda, E. (2014). TCCON data from Izaña (ES), Release GGG2014.R0. TCCON data archive, hosted by CaltechDATA, <https://doi.org/10.14291/tccon.ggg2014.izana01.R0/1149295>.
- Brynjarsdóttir, J. and O’Hagan, A. (2014). Learning about physical parameters: the importance of model discrepancy. *Inverse Problems*, 30:114007.
- Bukosa, B., Deutscher, N. M., Fisher, J. A., Kubistin, D. C., Paton-Walsh, C., and Griffith, D. W. (2019). Simultaneous shipborne measurements of CO₂, CH₄ and CO and their application to improving greenhouse-gas flux estimates in Australia. *Atmospheric Chemistry and Physics*, 19:7055–7072.
- Burrows, J. P., Hölzle, E., Goede, A. P. H., Visser, H., and Fricke, W. (1995). SCIAMACHY—Scanning Imaging Absorption Spectrometer for Atmospheric Cartography. *Acta Astronautica*, 35:445–451.
- Chevallier, F. (2007). Impact of correlated observation errors on inverted CO₂ surface fluxes from OCO measurements. *Geophysical Research Letters*, 34(L24804).
- Chevallier, F., Bréon, F.-M., and Rayner, P. J. (2007). Contribution of the Orbiting Carbon Observatory to the estimation of CO₂ sources and sinks: Theoretical study in a variational data assimilation framework. *Journal of Geophysical Research: Atmospheres*, 112(D9).
- Chevallier, F., Fisher, M., Peylin, P., Serrar, S., Bousquet, P., Bréon, F.-M., Chédin, A., and Ciais, P. (2005). Inferring CO₂ sources and sinks from satellite observations: Method and application to TOVS data. *Journal of Geophysical Research: Atmospheres*, 110(D24).
- Ciais, P., Rayner, P., Chevallier, F., Bousquet, P., Logan, M., Peylin, P., and Ramonet, M. (2010). Atmospheric inversions for estimating CO₂ fluxes: methods and perspectives. *Climatic Change*, 103:69–92.

- Connor, B. J., Boesch, H., Toon, G., Sen, B., Miller, C., and Crisp, D. (2008). Orbiting Carbon Observatory: Inverse method and prospective error analysis. *Journal of Geophysical Research: Atmospheres*, 113(D5).
- Cressie, N. and Wikle, C. (2011). *Statistics for Spatio-Temporal Data*. John Wiley and Sons, Hoboken, NJ.
- Crowell, S., Baker, D., Schuh, A., Basu, S., Jacobson, A. R., Chevallier, F., Liu, J., Deng, F., Feng, L., McKain, K., Chatterjee, A., Miller, J. B., Stephens, B. B., Eldering, A., Crisp, D., Schimel, D., Nassar, R., O'Dell, C. W., Oda, T., Sweeney, C., Palmer, P. I., and Jones, D. B. A. (2019). The 2015–2016 carbon cycle as seen from OCO-2 and the global in situ network. *Atmospheric Chemistry and Physics*, 19:9797–9831.
- Dahlén, U., Lindström, J., and Scholze, M. (2020). Spatiotemporal reconstructions of global CO₂-fluxes using Gaussian Markov random fields. *Environmetrics*, 31:e2610.
- Darmenov, A. and da Silva, A. (2015). The Quick Fire Emissions Dataset (QFED): Documentation of versions 2.1, 2.2 and 2.4, NASA Technical Report Series on Global Modeling and Data Assimilation. Technical Report TM-2015-104606, NASA.
- Datta, A., Banerjee, S., Finley, A. O., and Gelfand, A. E. (2016). Hierarchical nearest-neighbor Gaussian process models for large geostatistical datasets. *Journal of the American Statistical Association*, 111:800–812.
- De Mazière, M., Sha, M. K., Desmet, F., Hermans, C., Scolas, F., Kumps, N., Metzger, J.-M., Dufлот, V., and Cammas, J.-P. (2014). TCCON data from Réunion Island (RE), Release GGG2014.R0. TCCON data archive, hosted by CaltechDATA, <https://doi.org/10.14291/tcon.ggg2014.reunion01.R0/1149288>.
- Deng, F., Jones, D. B., O'Dell, C. W., Nassar, R., and Parazoo, N. C. (2016). Combining GOSAT XCO₂ observations over land and ocean to improve regional CO₂ flux estimates. *Journal of Geophysical Research: Atmospheres*, 121:1896–1913.
- Deutscher, N. M., Notholt, J., Messerschmidt, J., Weinzierl, C., Warneke, T., Petri, C., and Grupe, P. (2015). TCCON data from Bialystok (PL), Release GGG2014.R1. TCCON data archive, hosted by CaltechDATA, <https://doi.org/10.14291/tcon.ggg2014.bialystok01.R1/1183984>.
- Dlugokencky, E. and Tans, P. (2020). Trends in atmospheric carbon dioxide. National Oceanic & Atmospheric Administration, Earth System Research Laboratory (NOAA/ESRL). <http://www.esrl.noaa.gov/gmd/ccgg/trends>. last access: 2020-12-11.
- Dubey, M. K., Henderson, B. G., Green, D., Butterfield, Z. T., Keppel-Aleks, G., Allen, N. T., Blavier, J.-F., Roehl, C. M., Wunch, D., and Lindenmaier, R. (2014). TCCON data from Manaus (BR), Release GGG2014.R0. TCCON data archive, hosted by CaltechDATA, <https://doi.org/10.14291/tcon.ggg2014.manaus01.R0/1149274>.
- Edenhofer, O., R., Pichs-Madruga, Y., Sokona, E., Farahani, S., Kadner, K., Seyboth, A., Adler, I., Baum, S., Brunner, P., Eickemeier, B., Kriemann, J., Savolainen, S., Schlömer, C., von Stechow, T., Zwickel, and Minx, J. (2014). IPCC, 2014: Summary for Policymakers. In *Climate Change 2014: Mitigation of Climate Change. Contribution of Working Group III to the Fifth Assessment Report of the Intergovernmental Panel on Climate Change*. Cambridge University Press, Cambridge, UK.
- Eldering, A., O'Dell, C. W., Wennberg, P. O., Crisp, D., Gunson, M. R., Viatte, C., Avis, C., Braverman, A., Castano, R., Chang, A., Chapsky, L., Cheng, C., Connor, B., Dang, L., Doran, G., Fisher, B., Frankenberg, C., Fu, D., Granat, R., Hobbs, J., Lee, R. A. M., Mandrake, L., McDuffie, J., Miller, C. E., Myers, V., Natraj, V., O'Brien, D., Osterman, G. B., Oyafuso, F., Payne, V. H., Pollock, H. R., Polonsky, I., Roehl, C. M., Rosenberg, R., Schwandner, F., Smyth, M., Tang, V., Taylor, T. E., To, C., Wunch, D., and Yoshimizu, J. (2017). The Orbiting Carbon Observatory-2: First 18 months of science data products. *Atmospheric Measurement Techniques*, 10:549–563.

- Eldering, A., Taylor, T. E., O'Dell, C. W., and Pavlick, R. (2019). The OCO-3 mission: Measurement objectives and expected performance based on 1 year of simulated data. *Atmospheric Measurement Techniques*, 12:2341–2370.
- Engelen, R. J., Denning, A. S., and Gurney, K. R. (2002). On error estimation in atmospheric CO₂ inversions. *Journal of Geophysical Research: Atmospheres*, 107(D22):ACL–10.
- Enting, I. and Newsam, G. (1990). Atmospheric constituent inversion problems: Implications for baseline monitoring. *Journal of Atmospheric Chemistry*, 11:69–87.
- Enting, I. G. (2002). *Inverse Problems in Atmospheric Constituent Transport*. Cambridge University Press, Cambridge, UK.
- Fan, S., Gloor, M., Mahlman, J., Pacala, S., Sarmiento, J., Takahashi, T., and Tans, P. (1998). A large terrestrial carbon sink in North America implied by atmospheric and oceanic carbon dioxide data and models. *Science*, 282:442–446.
- Feist, D. G., Arnold, S. G., John, N., and Geibel, M. C. (2014). TCCON data from Ascension Island (SH), Release GGG2014.R0. TCCON data archive, hosted by CaltechDATA, <https://doi.org/10.14291/tccon.ggg2014.ascension01.r0/1149285>.
- Feng, L., Palmer, P., Bösch, H., and Dance, S. (2009). Estimating surface CO₂ fluxes from space-borne CO₂ dry air mole fraction observations using an ensemble Kalman filter. *Atmospheric Chemistry & Physics*, 9:2619–2633.
- Feng, S., Lauvaux, T., Keller, K., Davis, K. J., Rayner, P., Oda, T., and Gurney, K. R. (2019). A road map for improving the treatment of uncertainties in high-resolution regional carbon flux inverse estimates. *Geophysical Research Letters*, 46:13461–13469.
- Finley, A. O., Banerjee, S., Waldmann, P., and Ericsson, T. (2009). Hierarchical spatial modeling of additive and dominance genetic variance for large spatial trial datasets. *Biometrics*, 65:441–451.
- Ganesan, A. L., Rigby, M., Zammit-Mangion, A., Manning, A. J., Prinn, R. G., Fraser, P. J., Harth, C. M., Kim, K.-R., Krummel, P. B., Li, S., Mühle, J., O'Doherty, S. J., Park, S., Salameh, P. K., Steele, L. P., and Weiss, R. F. (2014). Characterization of uncertainties in atmospheric trace gas inversions using hierarchical Bayesian methods. *Atmospheric Chemistry and Physics*, 14:3855–3864.
- Giglio, L., Randerson, J. T., and van der Werf, G. R. (2013). Analysis of daily, monthly, and annual burned area using the fourth-generation global fire emissions database (GFED4). *Journal of Geophysical Research: Biogeosciences*, 118:317–328.
- Gneiting, T. and Raftery, A. E. (2007). Strictly proper scoring rules, prediction, and estimation. *Journal of the American Statistical Association*, 102:359–378.
- Griffith, D. W., Deutscher, N. M., Velazco, V. A., Wennberg, P. O., Yavin, Y., Keppel-Aleks, G., Washenfelder, R. A., Toon, G. C., Blavier, J.-F., Paton-Walsh, C., Jones, N. B., Kettlewell, G. C., Connor, B. J., Macatangay, R. C., Roehl, C., Ryzcek, M., Glowacki, J., Culfan, T., and Bryant, G. W. (2014a). TCCON data from Darwin (AU), Release GGG2014.R0. TCCON data archive, hosted by CaltechDATA, <https://doi.org/10.14291/tccon.ggg2014.darwin01.R0/1149290>.
- Griffith, D. W., Velazco, V. A., Deutscher, N. M., Paton-Walsh, C., Jones, N. B., Wilson, S. R., Macatangay, R. C., Kettlewell, G. C., Buchholz, R. R., and Rigggenbach, M. O. (2014b). TCCON data from Wollongong (AU), Release GGG2014.R0. TCCON data archive, hosted by CaltechDATA, <https://doi.org/10.14291/tccon.ggg2014.wollongong01.R0/1149291>.
- Gurney, K. R., Law, R. M., Denning, A. S., Rayner, P. J., Baker, D., Bousquet, P., Bruhwiler, L., Chen, Y.-H., Ciais, P., Fan, S., Fung, I. Y., Gloor, M., Heimann, M., Higuchi, K., John, J., Maki, T., Maksyutov, S., Masarie, K., Peylin, P., Prather, M., Pak, B. C., Randerson, J., Sarmiento, J., Taguchi, S., Takahashi, T., and Yuen, C.-W. (2002). Towards robust regional estimates of CO₂ sources and sinks using atmospheric transport models. *Nature*, 415:626–630.

- Hase, F., Blumenstock, T., Dohe, S., Groß, J., and Kiel, M. (2015). TCCON data from Karlsruhe (DE), Release GGG2014.R1. TCCON data archive, hosted by CaltechDATA, <https://doi.org/10.14291/tccon.ggg2014.karlsruhe01.R1/1182416>.
- Henderson, H. V. and Searle, S. R. (1981). On deriving the inverse of a sum of matrices. *Siam Review*, 23:53–60.
- Houweling, S., Aben, I., Breon, F.-M., Chevallier, F., Deutscher, N., Engelen, R., Gerbig, C., Griffith, D., Hungershofer, K., Macatangay, R., Marshall, J., Notholt, J., Peters, W., and Serrar, S. (2010). The importance of transport model uncertainties for the estimation of CO₂ sources and sinks using satellite measurements. *Atmospheric Chemistry and Physics*, 10:9981–9992.
- Houweling, S., Baker, D., Basu, S., Boesch, H., Butz, A., Chevallier, F., Deng, F., Dlugokencky, E. J., Feng, L., Ganshin, A., Hasekamp, O., Jones, D., Maksyutov, S., Marshall, J., Oda, T., O’Dell, C. W., Oshchepkov, S., Palmer, P. I., Peylin, P., Poussi, Z., Reum, F., Takagi, H., Yoshida, Y., and Zhuravlev, R. (2015). An intercomparison of inverse models for estimating sources and sinks of CO₂ using GOSAT measurements. *Journal of Geophysical Research: Atmospheres*, 120:5253–5266.
- Iraci, L. T., Podolske, J. R., Hillyard, P. W., Roehl, C., Wennberg, P. O., Blavier, J.-F., Landeros, J., Allen, N., Wunch, D., Zavaleta, J., Quigley, E., Osterman, G. B., Albertson, R., Dunwoody, K., and Boyden, H. (2016). TCCON data from Edwards (US), Release GGG2014.R1. TCCON data archive, hosted by CaltechDATA, <https://doi.org/10.14291/tccon.ggg2014.edwards01.r1/1255068>.
- Jacobson, A. R., Schuldt, K. N., Miller, J. B., Oda, T., Tans, P., Arlyn Andrews, Mund, J., Ott, L., Collatz, G. J., Aalto, T., Afshar, S., Aikin, K., Aoki, S., Apadula, F., Baier, B., Bergamaschi, P., Beyersdorf, A., Biraud, S. C., Bollenbacher, A., Bowling, D., Brailsford, G., Abshire, J. B., Chen, G., Chen, H., Chmura, L., Climadat, S., Colomb, A., Conil, S., Cox, A., Cristofanelli, P., Cuevas, E., Curcoll, R., Sloop, C. D., Davis, K., Wekker, S. D., Delmotte, M., DiGangi, J. P., Dlugokencky, E., Ehleringer, J., Elkins, J. W., Emmenegger, L., Fischer, M. L., Forster, G., Frumau, A., Galkowski, M., Gatti, L. V., Gloor, E., Griffis, T., Hammer, S., Haszpra, L., Hatakka, J., Heliasz, M., Hensen, A., Hermanssen, O., Hintsa, E., Holst, J., Jaffe, D., Karion, A., Kawa, S. R., Keeling, R., Keronen, P., Kolari, P., Kominkova, K., Kort, E., Krummel, P., Kubistin, D., Labuschagne, C., Langenfelds, R., Laurent, O., Laurila, T., Lauvaux, T., Law, B., Lee, J., Lehner, I., Leuenberger, M., Levin, I., Levula, J., Lin, J., Lindauer, M., Loh, Z., Lopez, M., Myhre, C. L., Machida, T., Mammarella, I., Manca, G., Manning, A., Manning, A., Marek, M. V., Marklund, P., Martin, M. Y., Matsueda, H., McKain, K., Meijer, H., Meinhardt, F., Miles, N., Miller, C. E., Mölder, M., Montzka, S., Moore, F., Morgui, J.-A., Morimoto, S., Munger, B., Necki, J., Newman, S., Nichol, S., Niwa, Y., O’Doherty, S., Ottosson-Löfvenius, M., Paplawsky, B., Peischl, J., Peltola, O., Pichon, J.-M., Piper, S., Plass-Dölmer, C., Ramonet, M., Reyes-Sanchez, E., Richardson, S., Riris, H., Ryerson, T., Saito, K., Sargent, M., Sasakawa, M., Sawa, Y., Say, D., Scheeren, B., Schmidt, M., Schmidt, A., Schumacher, M., Shepson, P., Shook, M., Stanley, K., Steinbacher, M., Stephens, B., Sweeney, C., Thoning, K., Torn, M., Turnbull, J., Tørseth, K., Bulk, P. V. D., Laan-Luijkx, I. T. V. D., Dintner, D. V., Vermeulen, A., Viner, B., Vitkova, G., Walker, S., Weyrauch, D., Wofsy, S., Worthy, D., Young, D., and Zimnoch, M. (2020). Carbontracker CT2019, Model published 2020 by NOAA Earth System Research Laboratory, Global Monitoring Division. https://www.esrl.noaa.gov/gmd/ccgg/carbontracker/CT2019_doc.php.
- Kaminski, T., Rayner, P. J., Heimann, M., and Enting, I. G. (2001). On aggregation errors in atmospheric transport inversions. *Journal of Geophysical Research: Atmospheres*, 106:4703–4715.
- Kawakami, S., Ohyama, H., Arai, K., Okumura, H., Taura, C., Fukamachi, T., and Sakashita, M. (2014). TCCON data from Saga (JP), Release GGG2014.R0. TCCON data archive, hosted by CaltechDATA, <https://doi.org/10.14291/tccon.ggg2014.saga01.R0/1149283>.
- Keller, C. A., Long, M. S., Yantosca, R. M., Da Silva, A. M., Pawson, S., and Jacob, D. J. (2014). HEMCO v1.0: A versatile, ESMF-compliant component for calculating emissions in atmospheric models. *Geoscientific Model Development*, 7:1409–1417.

- Kivi, R., Heikkinen, P., and Kyrö, E. (2014). TCCON data from Sodankylä (FI), Release GGG2014.R0. TCCON data archive, hosted by CaltechDATA, <https://doi.org/10.14291/tccon.ggg2014.sodankyla01.R0/1149280>.
- Kuze, A., Suto, H., Nakajima, M., and Hamazaki, T. (2009). Thermal and near infrared sensor for carbon observation Fourier-transform spectrometer on the Greenhouse Gases Observing Satellite for greenhouse gases monitoring. *Applied Optics*, 48:6716–6733.
- Lauvaux, T., Díaz-Isaac, L. I., Bocquet, M., and Bousseres, N. (2019). Diagnosing spatial error structures in CO₂ mole fractions and XCO₂ column mole fractions from atmospheric transport. *Atmospheric Chemistry & Physics*, 19(18).
- Lunt, M. F., Rigby, M., Ganesan, A. L., and Manning, A. J. (2016). Estimation of trace gas fluxes with objectively determined basis functions using reversible-jump Markov chain Monte Carlo. *Geoscientific Model Development*, 9:3213–3229.
- Masarie, K. A., Peters, W., Jacobson, A. R., and Tans, P. P. (2014). ObsPack: A framework for the preparation, delivery, and attribution of atmospheric greenhouse gas measurements. *Earth System Science Data*, 6:375–384.
- McNorton, J. R., Bousseres, N., Agustí-Panareda, A., Balsamo, G., Choulga, M., Dawson, A., Engelen, R., Kipling, Z., and Lang, S. (2020). Representing model uncertainty for global atmospheric CO₂ flux inversions using ECMWF-IFS-46R1. *Geoscientific Model Development*, 13:2297–2313.
- Michalak, A. M., Bruhwiler, L., and Tans, P. P. (2004). A geostatistical approach to surface flux estimation of atmospheric trace gases. *Journal of Geophysical Research*, 109:D14109.
- Michalak, A. M., Hirsch, A., Bruhwiler, L., Gurney, K. R., Peters, W., and Tans, P. P. (2005). Maximum likelihood estimation of covariance parameters for Bayesian atmospheric trace gas surface flux inversions. *Journal of Geophysical Research: Atmospheres*, 110(D24).
- Miller, S. M., Michalak, A. M., and Levi, P. J. (2014). Atmospheric inverse modeling with known physical bounds: an example from trace gas emissions. *Geoscientific Model Development*, 7:303–315.
- Miller, S. M., Saibaba, A. K., Trudeau, M. E., Mountain, M. E., and Andrews, A. E. (2020). Geostatistical inverse modeling with very large datasets: an example from the Orbiting Carbon Observatory 2 (OCO-2) satellite. *Geoscientific Model Development*, 13:1771–1785.
- Morino, I., Matsuzaki, T., and Horikawa, M. (2016). TCCON data from Tsukuba (JP), 125HR, Release GGG2014.R1. TCCON data archive, hosted by CaltechDATA, <https://doi.org/10.14291/tccon.ggg2014.tsukuba02.R1/1241486>.
- Mukherjee, C., Kasibhatla, P. S., and West, M. (2011). Bayesian statistical modeling of spatially correlated error structure in atmospheric tracer inverse analysis. *Atmospheric Chemistry and Physics*, 11:5365–5382.
- Nassar, R., Jones, D. B. A., Suntharalingam, P., Chen, J. M., Andres, R. J., Wecht, K. J., Yantosca, R. M., Kulawik, S. S., Bowman, K. W., Worden, J. R., Machida, T., and Matsueda, H. (2010). Modeling global atmospheric CO₂ with improved emission inventories and CO₂ production from the oxidation of other carbon species. *Geoscientific Model Development*, 3:689–716.
- Nassar, R., Napier-Linton, L., Gurney, K. R., Andres, R. J., Oda, T., Vogel, F. R., and Deng, F. (2013). Improving the temporal and spatial distribution of CO₂ emissions from global fossil fuel emission data sets. *Journal of Geophysical Research: Atmospheres*, 118:917–933.
- Neal, R. M. (2003). Slice sampling. *Annals of Statistics*, 31:705–741.
- Notholt, J., Petri, C., Warneke, T., Deutscher, N. M., Palm, M., Buschmann, M., Weinzierl, C., Macatangay, R. C., and Grupe, P. (2014). TCCON data from Bremen (DE), Release GGG2014.R0. TCCON data archive, hosted by CaltechDATA, <https://doi.org/10.14291/tccon.ggg2014.bremen01.R0/1149275>.

- Oda, T. and Maksyutov, S. (2011). A very high-resolution (1 km \times 1 km) global fossil fuel CO₂ emission inventory derived using a point source database and satellite observations of nighttime lights. *Atmospheric Chemistry and Physics*, 11:543–556.
- Oda, T., Maksyutov, S., and Andres, R. J. (2018). The Open-source Data Inventory for Anthropogenic CO₂, version 2016 (ODIAC2016): A global monthly fossil fuel CO₂ gridded emissions data product for tracer transport simulations and surface flux inversions. *Earth System Science Data*, 10:87–107.
- O’Dell, C. W., Connor, B., Bösch, H., O’Brien, D., Frankenberg, C., Castano, R., Christi, M., Eldering, D., Fisher, B., Gunson, M., McDuffie, J., Miller, C. E., Natraj, V., Oyafuso, F., Polonsky, I., Smyth, M., Taylor, T., Toon, G. C., Wennberg, P. O., and Wunch, D. (2012). The ACOS CO₂ retrieval algorithm Part 1: Description and validation against synthetic observations. *Atmospheric Measurement Techniques*, 5:99–121.
- O’Dell, C. W., Eldering, A., Wennberg, P. O., Crisp, D., Gunson, M. R., Fisher, B., Frankenberg, C., Kiel, M., Lindqvist, H., Mandrake, L., Merrelli, A., Natraj, V., Nelson, R. R., Osterman, G. B., Payne, V. H., Taylor, T. E., Wunch, D., Drouin, B. J., Oyafuso, F., Chang, A., McDuffie, J., Smyth, M., Baker, D. F., Basu, S., Chevallier, F., Crowell, S. M. R., Feng, L., Palmer, P. I., Dubey, M., García, O. E., Griffith, D. W. T., Hase, F., Iraci, L. T., Kivi, R., Morino, I., Notholt, J., Ohyama, H., Petri, C., Roehl, C. M., Sha, M. K., Strong, K., Sussmann, R., Te, Y., Uchino, O., and Velasco, V. A. (2018). Improved retrievals of carbon dioxide from Orbiting Carbon Observatory-2 with the version 8 ACOS algorithm. *Atmospheric Measurement Techniques*, 11:6539–6576.
- Peters, G. P., Andrew, R. M., Boden, T., Canadell, J. G., Ciais, P., Le Quéré, C., Marland, G., Raupach, M. R., and Wilson, C. (2013). The challenge to keep global warming below 2 °C. *Nature Climate Change*, 3:4–6.
- Peters, W., Miller, J., Whitaker, J., Denning, A., Hirsch, A., Krol, M., Zupanski, D., Bruhwiler, L., and Tans, P. (2005). An ensemble data assimilation system to estimate CO₂ surface fluxes from atmospheric trace gas observations. *Journal of Geophysical Research*, page D24304.
- Philip, S., Johnson, M. S., Potter, C., Genovesse, V., Baker, D. F., Haynes, K. D., Henze, D. K., Liu, J., and Poulter, B. (2019). Prior biosphere model impact on global terrestrial CO₂ fluxes estimated from OCO-2 retrievals. *Atmospheric Chemistry and Physics*, 19:13267–13287.
- Potter, C. S., Randerson, J. T., Field, C. B., Matson, P. A., Vitousek, P. M., Mooney, H. A., and Klooster, S. A. (1993). Terrestrial ecosystem production: a process model based on global satellite and surface data. *Global Biogeochemical Cycles*, 7:811–841.
- R Core Team (2020). *R: A Language and Environment for Statistical Computing*. R Foundation for Statistical Computing, Vienna, Austria. <https://www.R-project.org/>.
- Rasmussen, C. E. and Williams, C. K. I. (2006). *Gaussian Processes for Machine Learning*. The MIT Press, Cambridge, MA.
- Rayner, P. (2020). Data assimilation using an ensemble of models: A hierarchical approach. *Atmospheric Chemistry and Physics*, 20:3725–3737.
- Rayner, P. and O’Brien, D. (2001). The utility of remotely sensed CO₂ concentration data in surface source inversions. *Geophysical Research Letters*, 28:175–178.
- Rienecker, M. M., Suarez, M. J., Todling, R., Bacmeister, J., Takacs, L., Liu, H.-C., Gu, W., Sienkiewicz, M., Koster, R. D., Gelaro, R., Stajner, I., and Nielsen, J. (2008). The GEOS-5 Data Assimilation System—Documentation of Versions 5.0.1, 5.1.0, and 5.2.0. Technical Report TM–2008–104606, NASA.
- Rodgers, C. D. (2000). *Inverse Methods for Atmospheric Sounding*. World Scientific, Singapore, Singapore.
- Rodgers, C. D. and Connor, B. J. (2003). Intercomparison of remote sounding instruments. *Journal of Geophysical Research: Atmospheres*, 108(D3).

- Saeki, T., Maksyutov, S., Sasakawa, M., Machida, T., Arshinov, M., Tans, P., Conway, T. J., Saito, M., Valsala, V., Oda, T., Andres, R. J., and Belikov, D. (2013). Carbon flux estimation for Siberia by inverse modeling constrained by aircraft and tower CO₂ measurements. *Journal of Geophysical Research: Atmospheres*, 118:1100–1122.
- Schuh, A. E., Jacobson, A. R., Basu, S., Weir, B., Baker, D., Bowman, K., Chevallier, F., Crowell, S., Davis, K. J., Deng, F., Denning, S., Feng, L., Jones, D., Liu, J., and Palmer, P. I. (2019). Quantifying the impact of atmospheric transport uncertainty on CO₂ surface flux estimates. *Global Biogeochemical Cycles*, 33:484–500.
- Sherlock, V., Connor, B., Robinson, J., Shiona, H., Smale, D., and Pollard, D. F. (2014). TCCON data from Lauder (NZ), 125HR, Release GGG2014.R0. TCCON data archive, hosted by CaltechDATA, <https://doi.org/10.14291/tccon.ggg2014.lauder02.R0/1149298>.
- Strong, K., Roche, S., Franklin, J. E., Mendonca, J., Lutsch, E., Weaver, D., Fogal, P. F., Drummond, J. R., Batchelor, R., and Lindenmaier, R. (2016). TCCON data from Eureka (CA), Release GGG2014.R1. TCCON data archive, hosted by CaltechDATA, <https://doi.org/10.14291/tccon.ggg2014.eureka01.r1/1325515>.
- Takahashi, T., Sutherland, S. C., Sweeney, C., Poisson, A., Metzl, N., Tilbrook, B., Bates, N., Wanninkhof, R., Feely, R. A., Sabine, C., Olafsson, J., and Nojiri, Y. (2002). Global sea–air CO₂ flux based on climatological surface ocean pCO₂, and seasonal biological and temperature effects. *Deep Sea Research Part II: Topical Studies in Oceanography*, 49:1601–1622.
- Takahashi, T., Sutherland, S. C., Wanninkhof, R., Sweeney, C., Feely, R. A., Chipman, D. W., Hales, B., Friederich, G., Chavez, F., Sabine, C., Watson, A., Bakker, D. C. E., Schuster, U., Metzl, N., Yoshikawa-Inoue, H., Ishii, M., Midorikawa, T., Nojiri, Y., Körtzinger, A., Steinhoff, T., Hoppema, M., Olafsson, J., Arnarson, T. S., Tilbrook, B., Johannessen, T., Olsen, A., Bellerby, R., Wong, C. S., Delille, B., Bates, N. R., and de Baar, H. J. W. (2009). Climatological mean and decadal change in surface ocean pCO₂, and net sea–air CO₂ flux over the global oceans. *Deep Sea Research Part II: Topical Studies in Oceanography*, 56:554–577.
- Thoning, K. W., Crotwell, A. M., and Mund, J. W. (2020). Atmospheric carbon dioxide dry air mole fractions from continuous measurements at Mauna Loa, Hawaii, Barrow, Alaska, American Samoa and South Pole. 1973-2019, version 2020-08. <https://doi.org/10.15138/yaf1-bk21>.
- Tierney, L. (1994). Markov Chains for Exploring Posterior Distributions. *The Annals of Statistics*, 22:1701–1728.
- UNFCCC (2015). Adoption of the Paris Agreement. Report No. FCCC/CP/2015/L.9/Rev.1. <http://unfccc.int/resource/docs/2015/cop21/eng/109r01.pdf>.
- Vecchia, A. V. (1988). Estimation and model identification for continuous spatial processes. *Journal of the Royal Statistical Society: Series B*, 50:297–312.
- Warneke, T., Messerschmidt, J., Notholt, J., Weinzierl, C., Deutscher, N. M., Petri, C., and Grupe, P. (2014). TCCON data from Orléans (FR), Release GGG2014.R0. TCCON data archive, hosted by CaltechDATA, <https://doi.org/10.14291/tccon.ggg2014.orleans01.R0/1149276>.
- Wennberg, P. O., Roehl, C. M., Wunch, D., Toon, G. C., Blavier, J.-F., Washenfelder, R., Keppel-Aleks, G., Allen, N. T., and Ayers, J. (2014). TCCON data from Park Falls (US), Release GGG2014.R0. TCCON data archive, hosted by CaltechDATA, <https://doi.org/10.14291/tccon.ggg2014.parkfalls01.R0/1149161>.
- Wennberg, P. O., Wunch, D., Roehl, C. M., Blavier, J.-F., Toon, G. C., and Allen, N. T. (2015). TCCON data from Caltech (US), Release GGG2014.R1. TCCON data archive, hosted by CaltechDATA, <https://doi.org/10.14291/tccon.ggg2014.pasadena01.r1/1182415>.

- Wennberg, P. O., Wunch, D., Roehl, C. M., Blavier, J.-F., Toon, G. C., and Allen, N. T. (2016). TC-CON data from Lamont (US), Release GGG2014.R1. TCCON data archive, hosted by CaltechDATA, <https://doi.org/10.14291/tccon.ggg2014.lamont01.r1/1255070>.
- Wikle, C. K., Zammit-Mangion, A., and Cressie, N. (2019). *Spatio-Temporal Statistics with R*. CRC Press.
- Worden, J. R., Doran, G., Kulawik, S., Eldering, A., Crisp, D., Frankenberg, C., O’Dell, C., and Bowman, K. (2017). Evaluation and attribution of OCO-2 XCO₂ uncertainties. *Atmospheric Measurement Techniques*, 10:2759–2771.
- Wunch, D., Toon, G. C., Blavier, J.-F. L., Washenfelder, R. A., Notholt, J., Connor, B. J., Griffith, D. W., Sherlock, V., and Wennberg, P. O. (2011a). The Total Carbon Column Observing Network. *Philosophical Transactions of the Royal Society of London A: Mathematical, Physical and Engineering Sciences*, 369:2087–2112.
- Wunch, D., Toon, G. C., Wennberg, P. O., Wofsy, S. C., Stephens, B. B., Fischer, M. L., Uchino, O., Abshire, J. B., Bernath, P., Biraud, S. C., Blavier, J.-F. L., Boone, C., Bowman, K. P., Browell, E. V., Campos, T., Connor, B. J., Daube, B. C., Deutscher, N. M., Diao, M., Elkins, J. W., Gerbig, C., Gottlieb, E., Griffith, D. W. T., Hurst, D. F., Jiménez, R., Keppel-Aleks, G., Kort, E. A., Macatangay, R., Machida, T., Matsueda, H., Moore, F., Morino, I., Park, S., Robinson, J., Roehl, C. M., Sawa, Y., Sherlock, V., Sweeney, C., Tanaka, T., and Zondlo, M. A. (2010). Calibration of the Total Carbon Column Observing Network using aircraft profile data. *Atmospheric Measurement Techniques*, 3:1351–1362.
- Wunch, D., Wennberg, P. O., Toon, G. C., Connor, B. J., Fisher, B., Osterman, G. B., Frankenberg, C., Mandrake, L., O’Dell, C., Ahonen, P., Biraud, S. C., Castano, R., Cressie, N., Crisp, D., Deutscher, N. M., Eldering, A., Fisher, M. L., Griffith, D. W. T., Gunson, M., Heikkinen, P., Keppel-Aleks, G., Kyrö, E., Lindenmaier, R., Macatangay, R., Mendonca, J., Messerschmidt, J., Miller, C. E., Morino, I., Notholt, J., Oyafuso, F. A., Rettinger, M., Robinson, J., Roehl, C. M., Salawitch, R. J., Sherlock, V., Strong, K., Sussmann, R., Tanaka, T., Thompson, D. R., Uchino, O., Warneke, T., and Wofsy, S. C. (2011b). A method for evaluating bias in global measurements of CO₂ total columns from space. *Atmospheric Chemistry and Physics*, 11:12317–12337.
- Yantosca, B. (2019). geoschem/geos-chem: GEOS-Chem 12.3.2. <https://doi.org/10.5281/zenodo.2658178>.
- Yevich, R. and Logan, J. A. (2003). An assessment of biofuel use and burning of agricultural waste in the developing world. *Global Biogeochemical Cycles*, 17:1095.
- Zammit-Mangion, A., Cressie, N., and Ganesan, A. L. (2016). Non-Gaussian bivariate modelling with application to atmospheric trace-gas inversion. *Spatial Statistics*, 18:194–220.

A Markov chain Monte Carlo algorithm

As mentioned in Section 2.5, WOMBAT makes inference on the fluxes and the other parameters in the model using a Gibbs sampler, wherein samples of subsets of the parameters are iteratively drawn from their full conditional distributions (e.g., Tierney, 1994). Recall that the target distribution is $p(\boldsymbol{\alpha}, \boldsymbol{\beta}, \boldsymbol{\kappa}, \boldsymbol{\tau}_w, \boldsymbol{\theta}_{\xi, \epsilon} \mid \mathbf{Z}_2)$, as shown in (10), and that a graphical model that can be used for establishing conditional independence relationships is given in Figure 1.

The Gibbs sampler in WOMBAT is as follows. Given the i th sample, $\{\boldsymbol{\alpha}^{[i]}, \boldsymbol{\beta}^{[i]}, \boldsymbol{\kappa}^{[i]}, \boldsymbol{\tau}_w^{[i]}, \boldsymbol{\theta}_{\xi, \epsilon}^{[i]}\}$, the $(i + 1)$ th sample is generated sequentially in the following manner.

1. Sample $\boldsymbol{\alpha}^{[i+1]}$ and $\boldsymbol{\beta}^{[i+1]}$ jointly from $p(\boldsymbol{\alpha}, \boldsymbol{\beta} \mid \boldsymbol{\kappa}^{[i]}, \boldsymbol{\tau}_w^{[i]}, \boldsymbol{\theta}_{\xi, \epsilon}^{[i]}, \mathbf{Z}_2)$.
2. Sample $\boldsymbol{\kappa}^{[i+1]}$ from $p(\boldsymbol{\kappa} \mid \boldsymbol{\tau}_w^{[i]}, \boldsymbol{\alpha}^{[i+1]})$.
3. Sample $\boldsymbol{\tau}_w^{[i+1]}$ from $p(\boldsymbol{\tau}_w \mid \boldsymbol{\kappa}^{[i+1]}, \boldsymbol{\alpha}^{[i+1]})$.

4. Sample $\boldsymbol{\theta}_{\xi,\epsilon}^{[i+1]}$ from $p(\boldsymbol{\theta}_{\xi,\epsilon} \mid \boldsymbol{\alpha}^{[i+1]}, \boldsymbol{\beta}^{[i+1]}, \mathbf{Z}_2)$.

Below, in Sections A.1–A.4, we give the details for Steps 1–4. In deriving the conditional distributions, we often make use of the Sherman–Morrison–Woodbury matrix identity and a matrix-determinant lemma (e.g., Henderson and Searle, 1981). The former identity states that, for conformable matrices \mathbf{A} , \mathbf{U} , \mathbf{C} , and \mathbf{V} ,

$$(\mathbf{A} + \mathbf{UCV})^{-1} = \mathbf{A}^{-1} - \mathbf{A}^{-1}\mathbf{U}(\mathbf{C}^{-1} + \mathbf{VA}^{-1}\mathbf{U})^{-1}\mathbf{VA}^{-1},$$

whenever the required inverses exist, while the latter lemma states that

$$|\mathbf{A} + \mathbf{UCV}| = |\mathbf{C}^{-1} + \mathbf{VA}^{-1}\mathbf{U}||\mathbf{C}||\mathbf{A}|.$$

A.1 Sampling $\boldsymbol{\alpha}$ and $\boldsymbol{\beta}$

Let $\mathbf{B} = (\hat{\boldsymbol{\Psi}}, \mathbf{A})$, $\mathbf{x} = (\boldsymbol{\alpha}', \boldsymbol{\beta}')'$, and $\boldsymbol{\Sigma}_x = \text{bdiag}(\boldsymbol{\Sigma}_\alpha, \sigma_\beta^2 \mathbf{I})$. Then

$$\begin{aligned} p(\boldsymbol{\alpha}, \boldsymbol{\beta} \mid \boldsymbol{\kappa}, \tau_w, \boldsymbol{\theta}_{\xi,\epsilon}, \mathbf{Z}_2) \\ \propto \exp\left[-\frac{1}{2}(\mathbf{Z}_2 - \hat{\mathbf{Z}}_2^0 - \mathbf{B}\mathbf{x})'(\boldsymbol{\Sigma}_\xi + \boldsymbol{\Sigma}_\epsilon)^{-1}(\mathbf{Z}_2 - \hat{\mathbf{Z}}_2^0 - \mathbf{B}\mathbf{x}) - \frac{1}{2}\mathbf{x}'\boldsymbol{\Sigma}_x^{-1}\mathbf{x}\right]. \end{aligned}$$

The log of this quantity is quadratic in \mathbf{x} , and therefore the full conditional distribution of \mathbf{x} is a multivariate Gaussian distribution; specifically,

$$\mathbf{x} \mid \boldsymbol{\kappa}, \tau_w, \boldsymbol{\theta}_{\xi,\epsilon}, \mathbf{Z}_2 \sim \text{Gau}(\boldsymbol{\mu}_x^c, \boldsymbol{\Sigma}_x^c), \quad (19)$$

where

$$(\boldsymbol{\Sigma}_x^c)^{-1} = \mathbf{B}'(\boldsymbol{\Sigma}_\xi + \boldsymbol{\Sigma}_\epsilon)^{-1}\mathbf{B} + \boldsymbol{\Sigma}_x^{-1},$$

and

$$\boldsymbol{\mu}_x^c = \boldsymbol{\Sigma}_x^c \mathbf{B}'(\boldsymbol{\Sigma}_\xi + \boldsymbol{\Sigma}_\epsilon)^{-1}(\mathbf{Z}_2 - \hat{\mathbf{Z}}_2^0).$$

As described in Section 3, $\boldsymbol{\Sigma}_\epsilon$ is diagonal and, under Markov assumptions, $\boldsymbol{\Sigma}_\xi$ has a sparse inverse. These properties allow us to efficiently compute the required mean and covariance matrix through use of the Sherman–Morrison–Woodbury matrix identity. Once these are computed, sampling from (19) is straightforward.

A.2 Sampling $\boldsymbol{\kappa}$

The full conditional distribution of $\boldsymbol{\kappa}$ is

$$p(\boldsymbol{\kappa} \mid \tau_w, \boldsymbol{\alpha}) \propto |\boldsymbol{\Sigma}_\alpha|^{-1/2} \exp\left(-\frac{1}{2}\boldsymbol{\alpha}'\boldsymbol{\Sigma}_\alpha^{-1}\boldsymbol{\alpha}\right) p(\boldsymbol{\kappa}), \quad (20)$$

where, recalling Section 2.4, $p(\boldsymbol{\kappa})$ is a product of Beta density functions. Since each κ_j and $\tau_{w,j}$ is associated with a spatial region, we also partition $\boldsymbol{\alpha}$ by spatial region. That is, we define $\boldsymbol{\alpha} \equiv ((\boldsymbol{\alpha}^1)', \dots, (\boldsymbol{\alpha}^{r_s})')'$, where $\boldsymbol{\alpha}^j \in \mathbb{R}^{r_t}$, $j = 1, \dots, r_s$. For $j = 1, \dots, r_s$, the r_t -dimensional vector $\boldsymbol{\alpha}^j$ can therefore be associated with $\kappa_j, \tau_{w,j}$, and a $r_t \times r_t$ sub-block of the matrix $\boldsymbol{\Sigma}_\alpha^{-1}$, which we denote as $\boldsymbol{\Sigma}_{\alpha,j}^{-1}$. Under the autoregressive model in Section 2.4, $\boldsymbol{\Sigma}_{\alpha,j}^{-1} = \tau_{w,j} \mathbf{Q}_{\alpha,j}$, where

$$\mathbf{Q}_{\alpha,j} = \begin{pmatrix} 1 & -\kappa_j & & & \\ -\kappa_j & 1 + \kappa_j^2 & \ddots & & \\ & \ddots & \ddots & \ddots & \\ & & \ddots & 1 + \kappa_j^2 & -\kappa_j \\ & & & -\kappa_j & 1 \end{pmatrix}, \quad j = 1, \dots, r_s.$$

Since the flux scaling factors in each spatial region are treated as independent *a priori*, (20) may be written as $p(\boldsymbol{\kappa} \mid \boldsymbol{\tau}_w, \boldsymbol{\alpha}) = \prod_{j=1}^{r_s} p(\kappa_j \mid \boldsymbol{\tau}_{w,j}, \boldsymbol{\alpha}^j)$, where

$$p(\kappa_j \mid \boldsymbol{\tau}_{w,j}, \boldsymbol{\alpha}^j) \propto |\mathbf{Q}_{\alpha,j}|^{1/2} \exp\left(-\frac{\boldsymbol{\tau}_{w,j}}{2}(\boldsymbol{\alpha}^j)' \mathbf{Q}_{\alpha,j} \boldsymbol{\alpha}^j\right) \kappa_j^{a_{\kappa,j}-1} (1-\kappa_j)^{b_{\kappa,j}-1}. \quad (21)$$

To generate samples from (20), we therefore successively sample κ_j , $j = 1, \dots, r_s$, from its full conditional distribution (21). Equation (21) does not correspond to any standard distribution, so we use slice sampling (Neal, 2003) to sample from it.

A.3 Sampling $\boldsymbol{\tau}_w$

Similarly to $\boldsymbol{\kappa}$, the conditional distribution of $\boldsymbol{\tau}_w$ factorises across spatial regions, and it is therefore given by $p(\boldsymbol{\tau}_w \mid \boldsymbol{\kappa}, \boldsymbol{\alpha}) = \prod_{j=1}^{r_s} p(\tau_{w,j} \mid \kappa_j, \boldsymbol{\alpha}^j)$, where

$$p(\tau_{w,j} \mid \kappa_j, \boldsymbol{\alpha}^j) \propto \tau_{w,j}^{r_t/2} \exp\left(-\frac{\tau_{w,j}}{2}(\boldsymbol{\alpha}^j)' \mathbf{Q}_{\alpha,j} \boldsymbol{\alpha}^j\right) \tau_{w,j}^{\nu_{w,j}-1} e^{-\omega_{w,j} \tau_{w,j}}. \quad (22)$$

The density function in (22) is a Gamma density function,

$$\tau_{w,j} \mid \kappa_j, \boldsymbol{\alpha}^j \sim \text{Ga}(\nu_{w,j}^c, \omega_{w,j}^c), \quad (23)$$

where $\nu_{w,j}^c = \nu_{w,j} + \frac{1}{2}r_t$ and $\omega_{w,j}^c = \omega_{w,j} + \frac{1}{2}(\boldsymbol{\alpha}^j)' \mathbf{Q}_{\alpha,j} \boldsymbol{\alpha}^j$. Therefore, we sample from the full conditional distribution of $\boldsymbol{\tau}_w$ by successively sampling $\tau_{w,j}$, for $j = 1, \dots, r_s$, directly from (23).

A.4 Sampling $\boldsymbol{\theta}_{\xi,\epsilon}$

Since we assume that the parameters governing the correlated and uncorrelated error terms are data-group specific, the full conditional distribution of $\boldsymbol{\theta}_{\xi,\epsilon}$ is

$$p(\boldsymbol{\theta}_{\xi,\epsilon} \mid \boldsymbol{\alpha}, \boldsymbol{\beta}, \mathbf{Z}_2) \propto \prod_{g=1}^{n_g} p(\boldsymbol{\theta}_{\xi_g}, \gamma_g \mid \boldsymbol{\alpha}, \boldsymbol{\beta}, \mathbf{Z}_{2,g}), \quad (24)$$

where $p(\boldsymbol{\theta}_{\xi_g}, \gamma_g \mid \boldsymbol{\alpha}, \boldsymbol{\beta}, \mathbf{Z}_{2,g}) \propto p(\mathbf{Z}_{2,g} \mid \boldsymbol{\alpha}, \boldsymbol{\beta}, \boldsymbol{\theta}_{\xi_g}, \gamma_g) p(\boldsymbol{\theta}_{\xi_g}, \gamma_g)$; $p(\boldsymbol{\theta}_{\xi_g}, \gamma_g)$ is the joint prior over $\boldsymbol{\theta}_{\xi_g}$ and γ_g ; and

$$p(\mathbf{Z}_{2,g} \mid \boldsymbol{\alpha}, \boldsymbol{\beta}, \boldsymbol{\theta}_{\xi_g}, \gamma_g) \propto |\boldsymbol{\Sigma}_{\xi_g} + \boldsymbol{\Sigma}_{\epsilon_g}|^{-1/2} \exp\left[-\frac{1}{2}(\mathbf{Z}_{2,g} - \hat{\mathbf{Z}}_{2,g}^0 - \hat{\boldsymbol{\Psi}}_g \boldsymbol{\alpha} - \mathbf{A}_g \boldsymbol{\beta}_g)' (\boldsymbol{\Sigma}_{\xi_g} + \boldsymbol{\Sigma}_{\epsilon_g})^{-1} (\mathbf{Z}_{2,g} - \hat{\mathbf{Z}}_{2,g}^0 - \hat{\boldsymbol{\Psi}}_g \boldsymbol{\alpha} - \mathbf{A}_g \boldsymbol{\beta}_g)\right]. \quad (25)$$

The matrix operations in (25) may be computed efficiently using the matrix identities given at the start of this section. Since (25) does not correspond to any standard distribution, we use slice sampling to sample from it, for $g = 1, \dots, n_g$.

B Observation operator for OCO-2 retrievals

The retrieval algorithm used for OCO-2 takes spectral data as input and returns CO₂ mole fractions on 20 vertical levels as output via an optimisation procedure. The CO₂ mole fractions at these 20 vertical levels are subsequently used to compute a column-averaged CO₂ that we associate with a single retrieval. For the i th retrieval, denote the vector of retrieved mole fractions as $\mathbf{Z}_{2,i}^r$. Following the argument given by Rodgers and Connor (2003) and Connor et al. (2008), the retrieved mole fractions are given by

$$\mathbf{Z}_{2,i}^r = \mathbf{Y}_{2,i}^{0,r} + \mathbf{A}_i (\mathbf{Y}_{2,i} - \mathbf{Y}_{2,i}^{0,r}) + \boldsymbol{\varepsilon}_i^r,$$

where $\mathbf{Y}_{2,i}^{0,r} = (Y_{2,i,1}^{0,r}, \dots, Y_{2,i,20}^{0,r})'$ is the vector of prior-mean mole fractions used by the retrieval algorithm, specific to the i th retrieval (these are unrelated to the prior mean of the mole-fraction field used in our inversion, $Y_2^0(\cdot, \cdot, \cdot)$); \mathbf{A}_i is the ‘‘averaging kernel matrix’’; $\mathbf{Y}_{2,i} \equiv (Y_2(\mathbf{s}_i, h_{i,k}, t_i))_{k=1}^{20}$ is the true mole fraction at the 20 vertical levels for the retrieval at geopotential heights $h_{i,k}$, $k = 1, \dots, 20$; and $\boldsymbol{\varepsilon}_i^r$ is a vector of measurement errors (which may also include systematic biases and errors induced by nonlinearity in the inversion process). The column-averaged retrieval is then

$$Z_{2,i} = \mathbf{c}'_i \mathbf{Z}_{2,i}^r = Y_{2,i}^{0,rc} + \mathbf{c}'_i \mathbf{A}_i (\mathbf{Y}_{2,i} - \mathbf{Y}_{2,i}^{0,r}) + \mathbf{c}'_i \boldsymbol{\varepsilon}_i^r, \quad (26)$$

where $\mathbf{c}_i \equiv (c_{i,1}, \dots, c_{i,20})'$ are quadrature weights used to estimate the column average, and $Y_{2,i}^{0,rc} \equiv \mathbf{c}'_i \mathbf{Y}_{2,i}^{0,r}$ is the retrieval prior mean column-averaged CO₂. Define $\mathbf{a}_i \equiv (a_{i,1}, \dots, a_{i,20})'$, where

$$a_{i,k} \equiv \frac{1}{c_{i,k}} (\mathbf{c}'_i \mathbf{A}_i)_k, \quad k = 1, \dots, 20,$$

and $(\mathbf{c}'_i \mathbf{A}_i)_k$ denotes the k th element of $\mathbf{c}'_i \mathbf{A}_i$. The vector \mathbf{a}_i is the ‘‘averaging kernel vector’’ of the i th retrieval, which is available in the official releases of the OCO-2 data. It follows that the observation operator in (7) is defined as

$$\hat{\mathcal{A}}_i(Y_2(\mathbf{s}_i, \cdot, t_i)) \equiv Y_{2,i}^{0,rc} + \sum_{k=1}^{20} c_{i,k} a_{i,k} (Y_2(\mathbf{s}_i, h_{i,k}, t_i) - Y_{2,i,k}^{0,r}). \quad (27)$$

Note that we do not explicitly account for the error term $\mathbf{c}'_i \boldsymbol{\varepsilon}_i^r$ in our definition for $\hat{\mathcal{A}}_i$. This is because it will be absorbed by the error terms we use in the data model (8).

The averaging-kernel-vector elements $\{a_{i,k}\}$ are typically close in value to 1. They reflect the fact that the retrieval is not equally sensitive to the mole fractions at all the vertical levels. At levels where there is less sensitivity (i.e., values < 1), the retrieval prior-mean mole fraction will be assigned greater weight when producing the column-average CO₂ estimate (Rodgers, 2000).

C Supplementary Figures and Tables

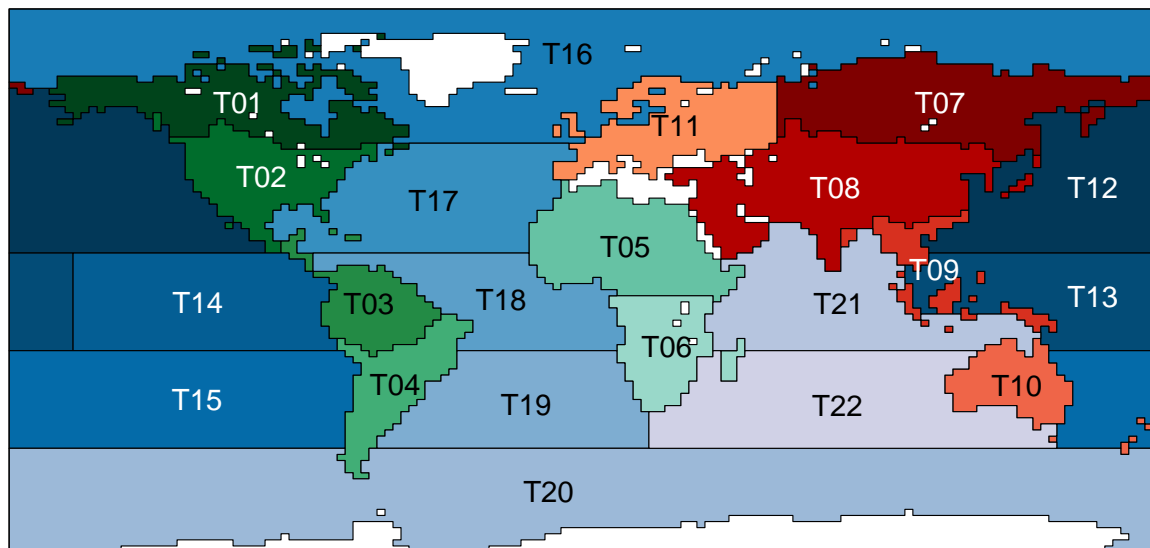


Fig. C1: Map of the 22 TransCom3 regions used in our study. The names of these regions are given in Table C1. The white regions correspond to areas assumed to have zero CO₂ surface flux.

Code	Name	Type
T01	North American Boreal	Land
T02	North American Temperate	Land
T03	Tropical South America	Land
T04	South American Temperate	Land
T05	Northern Africa	Land
T06	Southern Africa	Land
T07	Eurasia Boreal	Land
T08	Eurasia Temperate	Land
T09	Tropical Asia	Land
T10	Australia	Land
T11	Europe	Land
T12	North Pacific Temperate	Ocean
T13	West Pacific Tropical	Ocean
T14	East Pacific Tropical	Ocean
T15	South Pacific Temperate	Ocean
T16	Northern Ocean	Ocean
T17	North Atlantic Temperate	Ocean
T18	Atlantic Tropical	Ocean
T19	South Atlantic Temperate	Ocean
T20	Southern Ocean	Ocean
T21	Indian Tropical	Ocean
T22	South Indian Temperate	Ocean

Table C1: The code, name, and type, of the 22 TransCom3 regions used in our study. A map showing these regions is given in Figure C1.

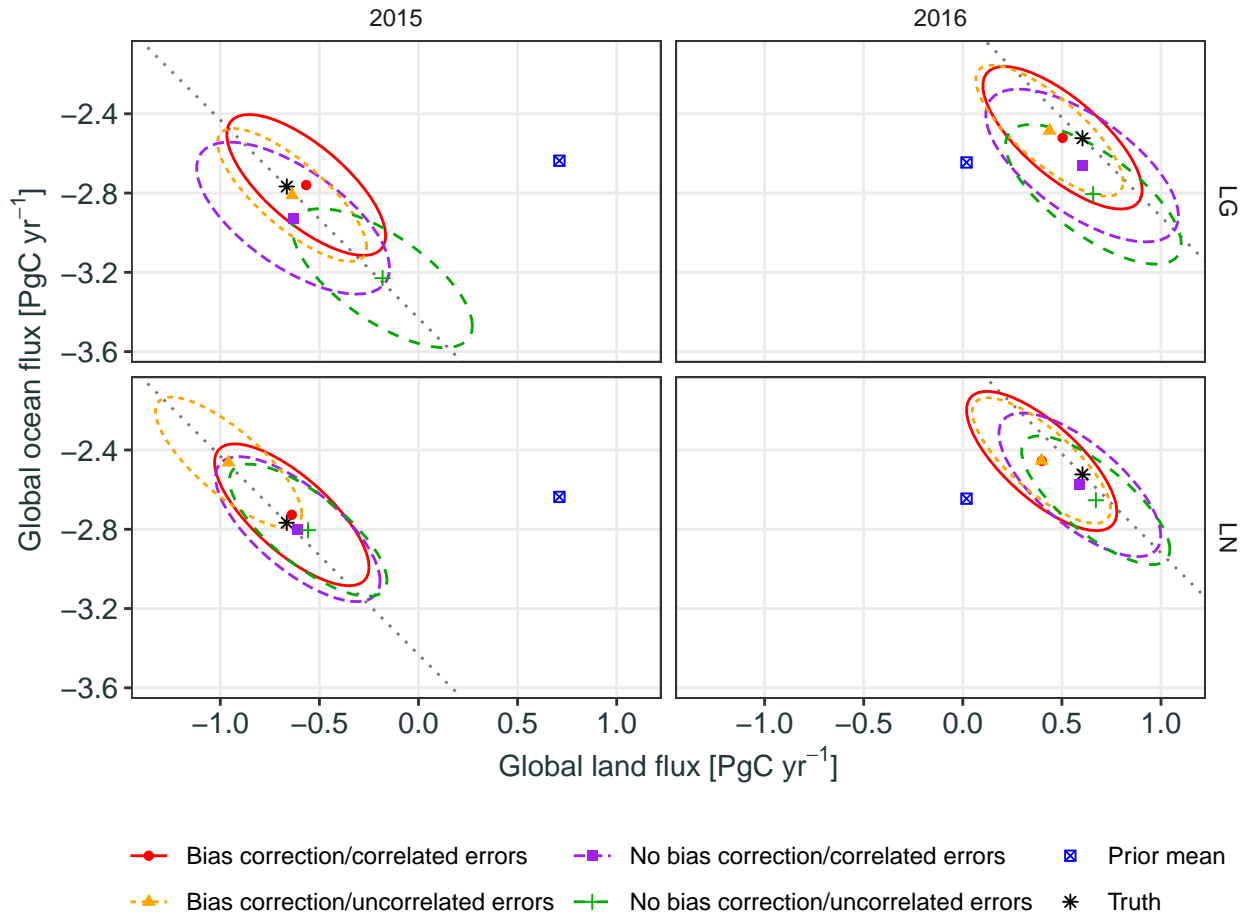


Fig. C2: As in Figure 3, but for Global ocean versus Global land.

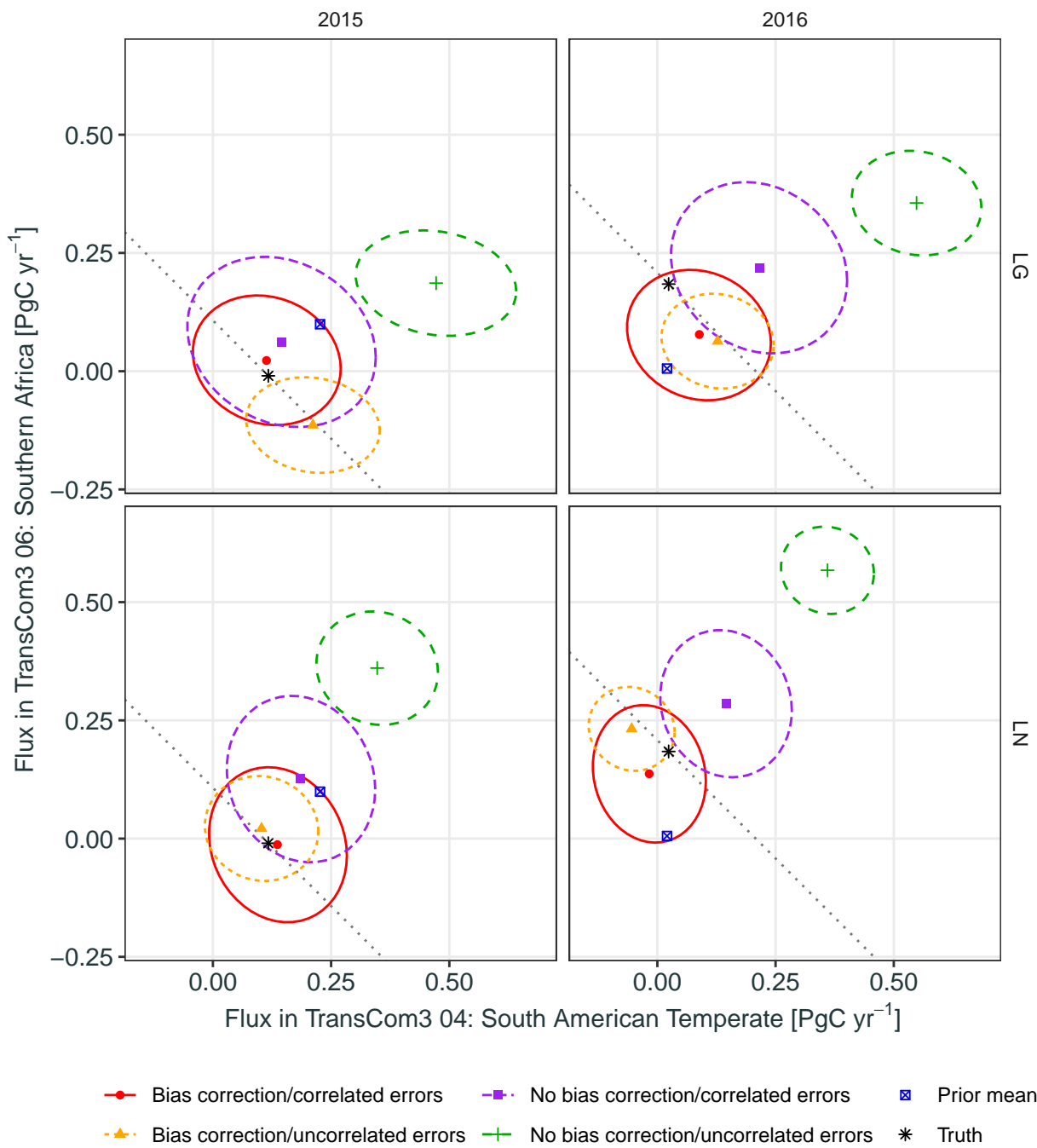


Fig. C3: As in Figure 3, but for the Southern Africa region (TransCom3 region 06) versus the South American Temperate region (TransCom3 region 04).

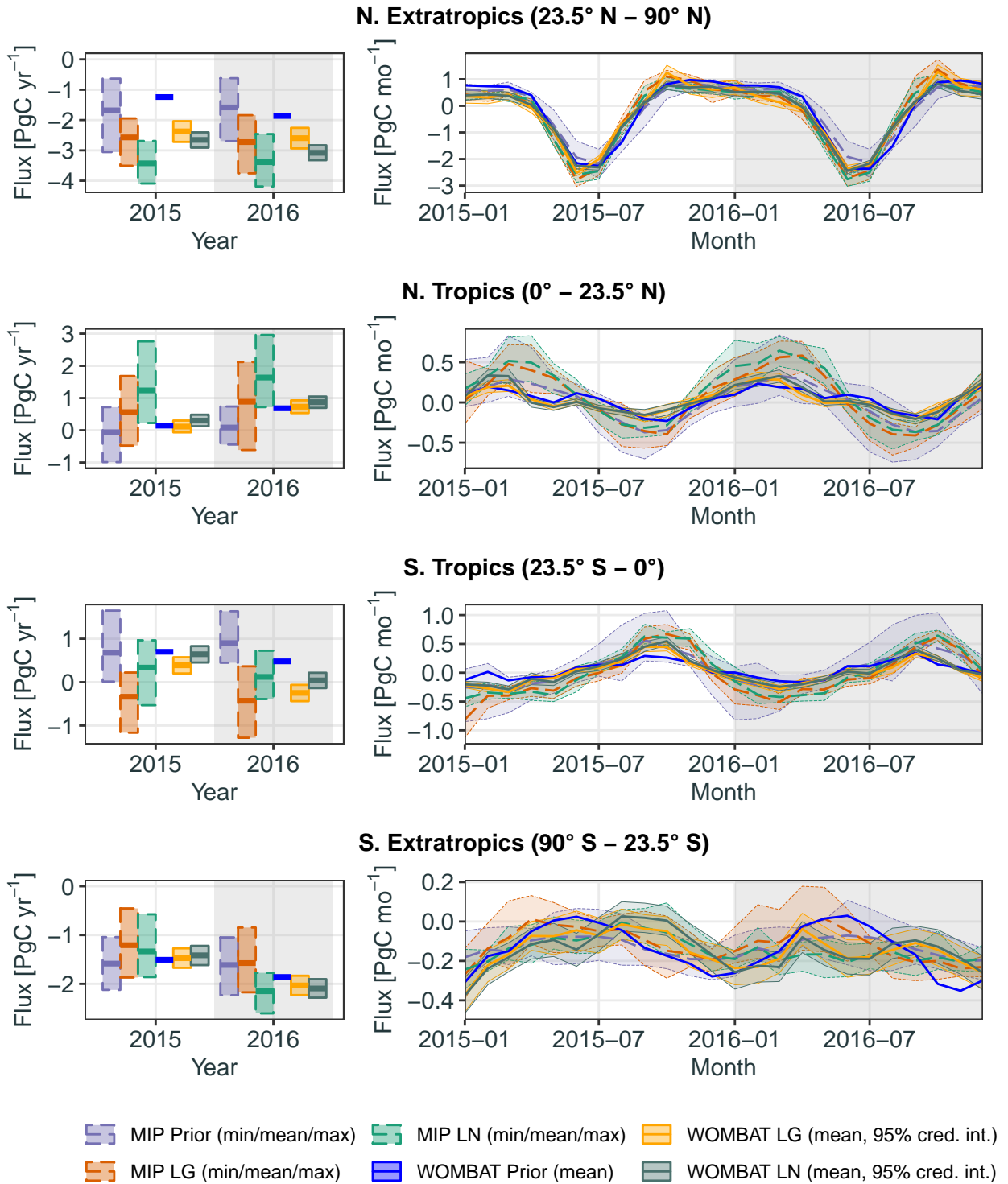


Fig. C4: As in Figure 4, but for zonal bands covering the northern extratropics (23.5°N–90°N), the northern tropics (0°–23.5°N), the southern tropics (23.5°S–0°), and the southern extratropics (90°S–23.5°S).

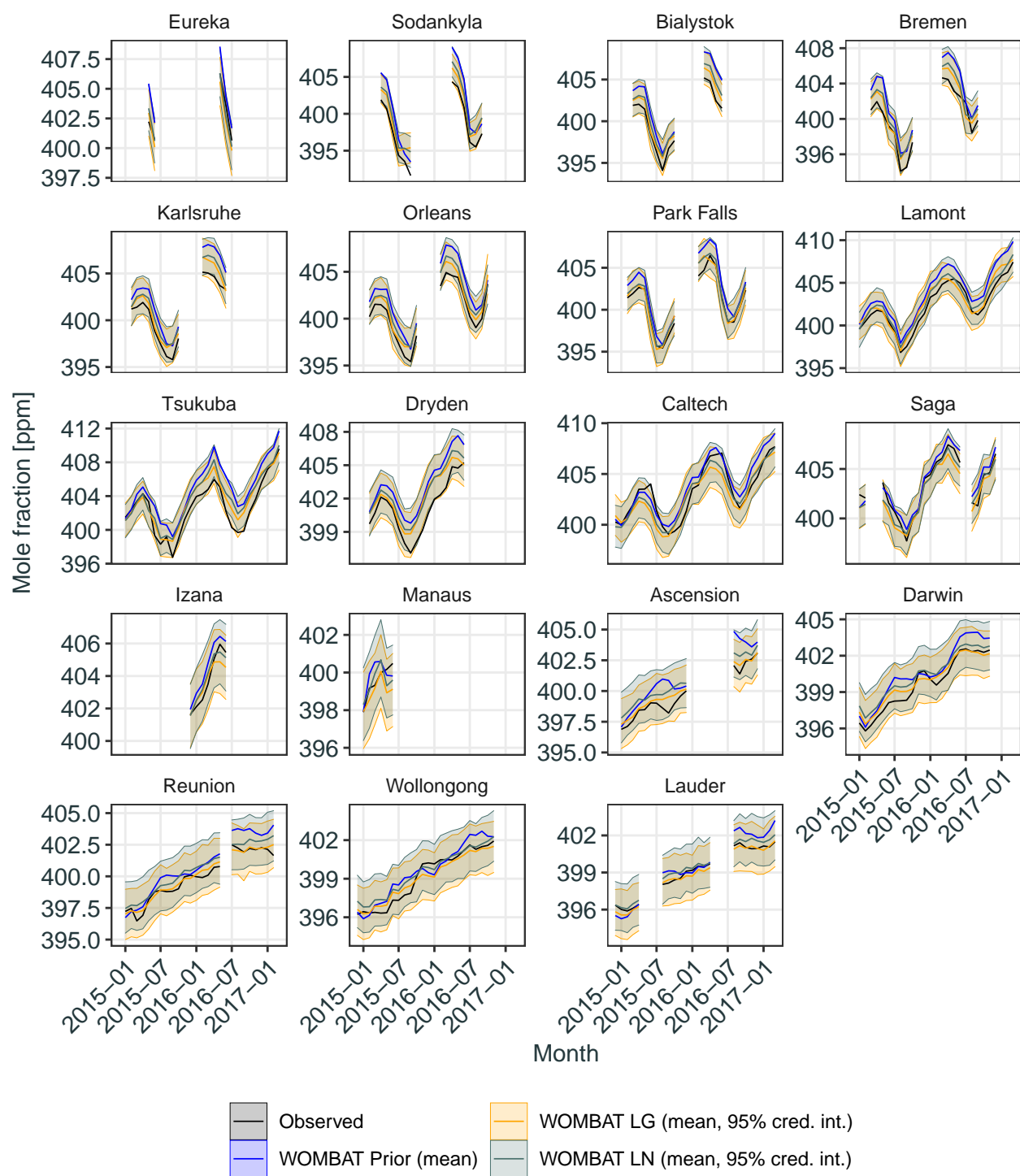


Fig. C5: Monthly-averaged TCCON retrievals together with the prior and posterior mole-fraction distributions from WOMBAT, by month and location. Each panel shows the quantities corresponding to a single site. Thick solid black lines show the TCCON retrievals, while thick coloured lines show the prior and posterior mole-fraction means. Shaded areas and thin lines show 95% posterior intervals for the cases “WOMBAT LG” and “WOMBAT LN.”